

A search for soft X-ray emission associated with prominent high-velocity-cloud complexes

J. Kerp^{1,2}, W.B. Burton³, R. Egger¹, M.J. Freyberg¹, Dap Hartmann^{4,2}, P.M.W. Kalberla², U. Mebold², and J. Pietz²

¹ Max-Planck-Institut für Extraterrestrische Physik, Postfach 1603, D-85740 Garching, Germany

² Radioastronomisches Institut der Universität Bonn, Auf dem Hügel 71, D-53121 Bonn, Germany

³ Sterrewacht Leiden, P.O. Box 9513, 2300 RA Leiden, The Netherlands

⁴ Harvard-Smithsonian Center for Astrophysics, 60 Garden Street, Cambridge, MA 02138, USA

Received 23 September 1996 / Accepted 7 October 1998

Abstract. We correlate the *ROSAT* $\frac{1}{4}$ keV all-sky survey with the Leiden/Dwingeloo H I survey, looking for soft X-ray signatures of prominent high-velocity-cloud (HVC) complexes. We study the transfer of $\frac{1}{4}$ keV photons through the interstellar medium in order to distinguish variations in the soft X-ray background (SXRb) intensity caused by photoelectric absorption effects from those due to excess X-ray emission. The X-ray data are modelled as a combination of emission from the Local Hot Bubble (LHB) and emission from a distant plasma in the galactic halo and extragalactic sources. The X-ray radiation intensity of the galactic halo and extragalactic X-ray background is modulated by the photoelectric absorption of the intervening galactic interstellar matter. We show that large- and small-scale intensity variations of the $\frac{1}{4}$ keV SXRb are caused by photoelectric absorption which is predominantly traced by the total N_{HI} distribution. The extensive coverage of the two surveys supports evidence for a hot, X-ray emitting corona. We show that this leads to a good representation of the SXRb observations. For four large areas on the sky, we search for regions where the modelled and observed X-ray emission differ. We find that there is excess X-ray emission towards regions near HVC complexes C, D, and GCN. We suggest that the excess X-ray emission is positionally correlated with the high-velocity clouds. Some lines of sight towards HVCs also pass through significant amounts of intermediate-velocity gas, so we cannot constrain the possible role played by IVC gas in these directions of HVC and IVC overlap, in determining the X-ray excesses.

Key words: ISM: clouds – Galaxy: halo – Galaxy: kinematics and dynamics – X-rays: ISM

1. Introduction

High-velocity clouds are H I structures characterized by radial velocities which deviate typically by several hundred km s^{-1} from conventional galactic rotation (see Wakker & van Woerden (1997) for a recent review). Distances remain uncertain for most of the clouds. Distance limits have been constrained for

only two lines of sight by optical absorption lines found by Danly et al. (1993) and by van Woerden et al. (1998) toward complexes M ($d < 5$ kpc) and A ($4 < d < 10$ kpc). There is consensus that the HVCs comprising the Magellanic Stream are at Magellanic Cloud distances ($\simeq 50$ kpc), based on positional and kinematic coincidences and the ability of tidal models to account for these coincidences. But the matter of distances remains largely unresolved for the majority of the HVCs. Blitz et al. (1998) suggest that some HVCs are scattered throughout the Local Group, excepting the principal northern complexes and the Magellanic Stream. Morphological arguments have led several authors (e.g. Hirth et al. 1985) to suggest that some HVCs interact with the galactic disk. This scenario is supported by the detection of soft X-ray enhancements close to HVC complexes M (Herbstmeier et al. 1995) and C (Hirth et al. 1985; Kerp et al. 1994, 1995, 1996). In addition, evidence of a physical connection of some HVCs with the galactic disk has been found in the H I “velocity bridges” which seem to link the HVC gas with gas at conventional velocities (Pietz et al. 1996).

We extend the SXRb investigations of Herbstmeier et al. (1995) and Kerp et al. (1996) to other HVC complexes, different in location, velocity, and possibly in origin, we use correlations of *ROSAT* $\frac{1}{4}$ keV X-ray data (see Snowden et al. 1997) with data from the Leiden/Dwingeloo H I survey (Hartmann & Burton 1997). The selected fields are at high latitudes, widely distributed over the sky, which encompass readily identifiable (see Wakker & van Woerden 1997) parts of HVC complexes. The complexes C, A, D, WA, and GCN fit those criteria; the detailed shapes of the selected fields were partly determined by the polar-grid projection of the *ROSAT* data.

We evaluate the transmission of $\frac{1}{4}$ keV photons through the X-ray absorbing interstellar medium, and demonstrate that the transmission is quantitatively traced by H I. Our approach aims at distinguishing fluctuations in the soft X-ray intensities caused by photoelectric absorption effects from those signifying true excess soft X-ray emission. To this end, we first model the SXRb distribution modulated by the photoelectric absorption caused by Milky Way gas at conventional and intermediate velocities. We then subtract the modelled SXRb distribution from the ob-

Table 1. Location of the HVC fields selected, and the N_{HI} and X-ray count rate ranges encountered in each field. The mean *ROSAT* integration times, $t_{\text{X-ray}}$, are also given, with minimum and maximum times noted in parentheses.

complex	l -range	b -range	N_{HI} (10^{20} cm^{-2})	$I_{1/4 \text{ keV}}$ ($10^{-4} \text{ cts s}^{-1} \text{ arcmin}^{-2}$)	$t_{\text{X-ray}}$ (seconds)
GCN	18° – 73°	-52° – -15°	2.0–12.0	0.7–12.0	460 (170–680)
C low, D	34° – 86°	$+33^\circ$ – $+79^\circ$	0.6–11.5	2.6–20.8	1000 (262–3200)
WA	218° – 270°	$+24^\circ$ – $+52^\circ$	1.5–7.9	3.0–12.7	530 (331–714)
C high	99° – 166°	$+12^\circ$ – $+74^\circ$	0.3–19.3	2.1–44.6	750 (244–3514)

served one, and identify regions where the modelled distribution deviates from what is observed.

In Sect. 2, we describe the X-ray and H I data used. In Sect. 3, we evaluate the soft X-ray radiation-transfer equation with the goal of finding HVC signatures in the SXR distribution. In Sect. 4, we show the results of the correlation analysis towards individual HVC complexes. In Sect. 5, we discuss the implications for the origin and distribution of the SXR sources. The results are summarized in Sect. 6.

2. X-ray and H I data

The X-ray data were obtained from the *ROSAT* all-sky survey (Snowden & Schmitt 1990; Voges 1992; Snowden et al. 1997). Photon events detected by the Position Sensitive Proportional Counter (PSPC; Pfeiffermann et al. 1986) were binned into seven pulse-height channels (R1–R7; Snowden et al. 1994a) covering the entire *ROSAT* PSPC energy window. The SXR radiation between $0.1 \text{ keV} \leq E \leq 0.28 \text{ keV}$ was measured in the R1 and R2 bands. Combining the R1 and R2 bands to produce the *ROSAT* $\frac{1}{4}$ keV data offers the highest statistical significance of soft X-ray material available. The $\frac{1}{4}$ keV energy range is the most sensitive of the *ROSAT* PSPC bands to photoelectric absorption by the interstellar medium. In this band the interstellar absorption cross section is about $\sigma_{\text{X}} \simeq 10^{-20} \text{ cm}^2 \text{ H I}^{-1}$. In consequence, the product of soft X-ray absorption cross section and the H I column density, N_{HI} , is close to or greater than unity across the sky, with the exception of a few lines of sight. The data are corrected for scattered solar X-rays (Snowden & Freyberg 1993), as well as for particle background (Plucinsky et al. 1993) and long-term X-ray enhancements (Snowden et al. 1995). The full intrinsic angular resolution of the PSPC has been used, yielding maps with $12'$ resolution; point sources have been removed to a minimum count rate of 0.02 cts s^{-1} (Snowden et al. 1997).

The H I data are those of the Leiden/Dwingeloo survey of Hartmann & Burton (1997), who used the Dwingeloo 25-m telescope to observe the sky at $\delta \geq -30^\circ$ with a true-angle grid spacing of $0.5'$ in both l and b . The velocity resolution is set by the interval of 1.03 km s^{-1} between each of the 1024 channels of the spectrometer; the material covers LSR velocities between -450 km s^{-1} and $+400 \text{ km s}^{-1}$, and thus encompasses essentially all HVC emission. The rms limit on the measured brightness-temperature fluctuations is $\Delta T_{\text{B}} = 0.07 \text{ K}$. The cor-

rection for stray radiation is described by Hartmann et al. (1996). The H I data are published as FITS files on a CD-ROM by Hartmann & Burton (1997), together with an atlas of maps.

Table 1 summarizes the main parameters of the regions studied as well as their typical X-ray intensities and H I column densities. We projected the N_{HI} distribution, regridded to an angular resolution of $48'$, onto the polar-grid projection of the *ROSAT* survey. The choice of angular resolution aimed at enhancing the statistical significance of the X-ray data and allowing differentiation between systematic uncertainties introduced by X-ray raw-data processing (e.g. residual point source contributions and scanning stripes) and modelling of the X-ray intensity distribution. The statistical significance, σ (corresponding to the uncertainty within a $48' \times 48'$ area), of soft X-ray enhancements and depressions was evaluated using the *ROSAT* uncertainty maps, which account only for the number of photon events: they do not include any systematic uncertainties introduced by non-cosmic X-ray backgrounds.

3. Radiation transfer of the soft X-rays

Earlier investigations of the *ROSAT* data (Snowden et al. 1994b; Herbstmeier et al. 1995; Kerp et al. 1996) indicated that the brightnesses from both, the distant X-ray sources and from the Local Hot Bubble (LHB) vary across the sky. Because of the variations of both source terms, we first address some general properties of the $\frac{1}{4}$ keV radiation transfer through the interstellar medium before attempting to identify imprints of HVCs on the SXR radiation. We focus on the following questions:

1. Are there significant variations of the SXR source distribution on scales of 0.8° to tens of degrees?
2. Is H I alone the tracer of the soft X-ray absorption by neutral matter? Do the H I/X-ray results require diffusely distributed H_2 and/or H^+ at high $|b|$ as additional tracers of soft X-ray absorption?
3. Can the velocity range of galactic H I accounting for the SXR absorption be constrained: does the gas at conventional and intermediate galactic velocities suffice, or are HVCs also implicated?

To answer these questions, we sought an expression for the soft X-ray radiation-transfer equation which reveals simultaneously the intensity and positional distribution of the individual source terms.

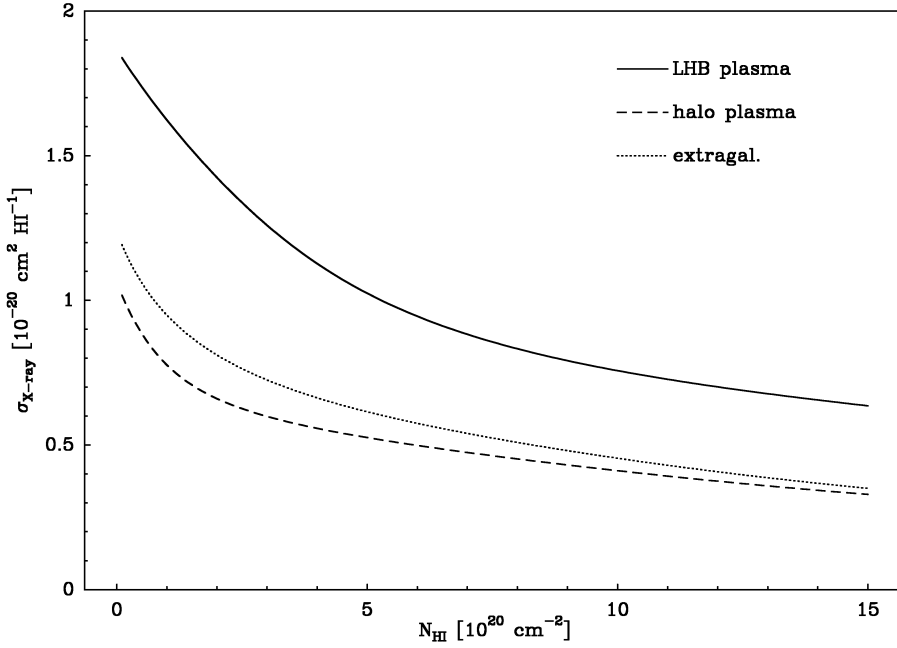


Fig. 1. *ROSAT* $\frac{1}{4}$ keV photoelectric absorption cross section (Morrison & McCammon 1983) versus N_{HI} . The effective cross section (σ_X) depends on the X-ray spectrum. The solid line shows σ_X (LHB) for the LHB plasma with $T_{\text{LHB}} = 10^{5.85}$ K; the dashed line shows σ_X (halo) for the distant galactic plasma with $T_{\text{halo}} = 10^{6.3}$ K, based on the Raymond & Smith (1977) plasma code. The dotted line shows σ_X (extragal) for the extragalactic power-law spectrum of $E^{-1.5}$ (Gendreau et al. 1995).

3.1. The soft X-ray radiation-transfer equation

The soft X-ray intensity distribution is modulated by photoelectric absorption due to interstellar matter lying between the observer and the source of the X-rays. The effective photoelectric absorption cross section (σ_X) depends on the chemical composition of the absorbing matter, normalized to a mean absorption cross section per neutral hydrogen atom (Morrison & McCammon 1983). Moreover, the absolute value of this cross section depends on the source spectrum and on the sensitivity function (bandpass) of the X-ray detector system. These dependences stem from the energy dependence of the absorption cross section ($\sigma_X \propto E^{-\frac{8}{3}}$). This leads to stronger attenuation for the lower-energy X-ray photons than for the more energetic ones. The more absorbing matter is located along the line of sight the stronger the softer-energy end is attenuated relative to the harder-energy end. This situation leads to an apparent hardening of the source X-ray spectrum due to photoelectric absorption.

The dependence of photoelectric absorption cross section on N_{HI} is shown in Fig. 1 for the LHB, for a galactic halo plasma, and for a power-law extragalactic X-ray spectrum. We discuss below the X-ray source spectra of these three components. At high $|b|$, the *ROSAT* PSPC data suggest that, in addition to emission from the LHB, diffusely distributed X-ray emission originates beyond the bulk of the galactic H I gas layer (Herbstmeier et al. 1995; Kerp et al. 1996; Pietz et al. 1998a, 1998b; Wang 1998). This situation requires at least two source terms in the radiation-transfer equation.

The X-ray emission from the LHB evidently originates from a thermal plasma (I_{LHB} ; McCammon & Sanders 1990), embedded in the local void of neutral matter. The local interstellar cavity is evidently an irregularly-shaped, low-volume-density region enclosing the solar neighborhood, where the X-ray in-

tensity varies (roughly proportionally to the pathlength, in the range of 50 to 150 pc, through the local cavity) on scales of several tens of degrees (Cox & Reynolds 1987; Egger et al. 1996).

The distant soft X-ray emission is most likely the superposition of thermal plasma radiation (I_{halo} ; Kerp 1994; Sidher et al. 1996) from the galactic halo (Pietz et al. 1998a, 1998b) and emission from unresolved extragalactic point sources building up the extragalactic soft X-ray background (I_{extragal} ; Hasinger et al. 1993). Accordingly, the soft X-ray transfer equation has the form:

$$I_{\text{SXR}} = I_{\text{LHB}} \cdot e^{-\sigma_X(\text{LHB}) \cdot N_{\text{HI}}(\text{LHB})} + I_{\text{halo}} \cdot e^{-\sigma_X(\text{halo}) \cdot N_{\text{HI}}(\text{total})} + I_{\text{extragal}} \cdot e^{-\sigma_X(\text{extragal}) \cdot N_{\text{HI}}(\text{total})} \quad (1)$$

3.2. The spectral properties of the distant source terms

The LHB term represents the thermal plasma radiation of the local gas. The intensity of the LHB varies across the entire sky: $I_{\text{LHB}} = (2.5 - 8.2) \cdot 10^{-4}$ cts $\text{s}^{-1} \text{arcmin}^{-2}$ (Snowden et al. 1998). The distant soft X-ray term represents the superposition of the isotropically distributed intensity of the extragalactic background radiation and the distant galactic plasma radiation. The unabsorbed X-ray intensity contributed by the extragalactic radiation is about $I_{\text{extragal}} = (2.3 - 4.4) \cdot 10^{-4}$ cts $\text{s}^{-1} \text{arcmin}^{-2}$ (Barber et al. 1996; Cui et al. 1996) while the unabsorbed distant X-ray intensity (assuming a patchy galactic X-ray halo) is about $I_{\text{halo}} = (4.0 - 30) \cdot 10^{-4}$ cts $\text{s}^{-1} \text{arcmin}^{-2}$ (Snowden et al. 1998). Thus, the distant galactic X-ray plasma will be of prime importance in studying $I_{\text{distant}} = I_{\text{halo}} + I_{\text{extragal}}$ because it is the source term with the largest intensity range and with an unknown distribution across the fields of interest.

It is plausible to assume that all of the galactic ISM is available to absorb radiation from the extragalactic SXR component. Pietz et al. (1998b) derive an exponential scale height of $h_z \sim 4.4$ kpc for the X-ray emitting halo, while Lockman & Gehman (1991) showed most of the conventional-velocity galactic H I gas is located at $|z| \lesssim 0.4$ kpc.

3.2.1. The source spectrum of I_{halo}

The galactic halo X-ray emission is evidently due to thermal-plasma processes. Rocchia et al. (1984) found plasma emission from O^{+6} and O^{+7} ions. Hasinger (1991) found indications in deep PSPC observations for an emission bump in the X-ray spectrum near 0.6 keV, also indicating the presence of these ions. Kerp (1994) and Sidher et al. (1996) showed that a thermal-plasma spectrum fits PSPC data well. The PSPC data suggest that the distant X-ray plasma, approximated by the Raymond & Smith (1977) model, has a temperature $T_{\text{plasma}} = 10^{6.3 \pm 0.1}$ K. In view of these results and of those of Pietz et al. (1998b), we assume that the galactic halo plasma is in collisionally ionized equilibrium. (This assumption is a simplification of the plasma processes occurring at high $|z|$, but is reasonable despite lacking detailed information about the X-ray spectrum.) Note that near $T \sim 10^{6.3}$ K, the absorption cross-section in the $\frac{1}{4}$ keV band does not depend strongly on plasma temperature (Snowden et al. 1997).

3.2.2. The source spectrum of I_{extragal}

I_{extragal} is caused by the superposition of X-rays from extragalactic point sources (Hasinger et al. 1998). The spectrum of the extragalactic background is a matter of discussion (Gendreau et al. 1995; Georgantopoulos et al. 1996). The averaged spectrum of bright, discrete soft X-ray sources, together providing the extragalactic background in the *ROSAT* energy window, can be approximated by a power law ($E^{-\Gamma}$) with an averaged spectral index of 2.1–2.2 (Hasinger et al. 1993, 1998). At lower fluxes, the contribution of faint emission-line galaxies dominates the spectral properties of the extragalactic background, leading to a flatter power-law slope (Almaini et al. 1996). Our investigation of the SXR deals with lower source fluxes than those investigated by Almaini et al.; accordingly, a plausible value of the extragalactic spectral index is $\Gamma \simeq 1.5$ (Gendreau et al. 1995).

3.3. The simplified soft X-ray radiation-transfer equation

We show that we may simplify Eq. (1) into an expression involving only two X-ray source terms for the $\frac{1}{4}$ keV band, namely the LHB source term (I_{LHB}) and the distant source term (I_{distant}), representing the superposition of the thermal plasma emission beyond the bulk of the galactic H I and the extragalactic background radiation: ($I_{\text{distant}} = I_{\text{halo}} + I_{\text{extragal}}$).

3.3.1. The I_{LHB} source term

The LHB source term varies approximately in proportion to the extent of the local cavity (Snowden et al. 1998). The *ROSAT* X-ray data considered here are limited in sensitivity (at the $3\text{-}\sigma$ level) to N_{HI} variations of about $N_{\text{HI}} \sim 5 \cdot 10^{19} \text{ cm}^{-2}$. The moderate angular resolution of the data we chose limits the angular extent of the small-scale intensity variations, anti-correlated to small-scale N_{HI} variations, to about $48'$. Thus, a narrow H I filament with $N_{\text{HI}} \leq 5 \cdot 10^{19} \text{ cm}^{-2}$ will not be detectable. Taking these limitations into account, interstellar absorption-line measurements (Welsh et al. 1998) show that properties of the local cavity vary smoothly on angular scales of several tens of degrees. Therefore, I_{LHB} reveals a distribution of soft X-rays approximately smooth over tens of degrees. We start our analysis using the assumption that across each individual field $I_{\text{LHB}} = \text{const.}$, and then show below that this conforms to the observed situation.

Because the effective photoelectric absorption cross section of the LHB plasma is larger than that of the galactic-halo plasma and of the extragalactic power-law spectrum (Fig. 1), deviations from the assumption of $I_{\text{LHB}} = \text{const.}$ will be easily detected. A local cloud attenuating soft X-rays will be disclosed by a deeper soft X-ray shadow than would be the case if the same cloud were located outside the LHB (see Kerp & Pietz 1998).

3.3.2. The I_{distant} source term

The I_{distant} source term represents the sum of I_{halo} and I_{extragal} . Fig. 1 suggests that the photoelectric absorption cross sections of the halo plasma and the extragalactic power-law spectrum have comparable values. The largest difference between the cross sections, amounting to some 20%, occurs in the range $N_{\text{HI}} = 1 - 3 \cdot 10^{20} \text{ cm}^{-2}$. Evaluating ($e^{-\sigma_{\text{X}}(\text{halo,extragal}) \cdot N_{\text{HI}}}$), we see that such a difference corresponds to a 7% effect on I_{distant} , which is negligible to our purposes in view of the statistical limitations of the X-ray data. Moreover, as we show below (see Fig. 7), $I_{\text{halo}} > I_{\text{extragal}}$ in most regions of the high- $|b|$ sky, so that the influence of the difference between the cross sections is reduced in proportion to the intensity contrast of both source terms. Hence we assume, for our purposes, that $\sigma_{\text{distant}} \simeq \sigma_{\text{halo}} \simeq \sigma_{\text{extragal}}$ towards high $|b|$.

We assume thus that $I_{\text{LHB}} = \text{const.}$ within each field examined. Deviations from this assumption will be revealed by failures of our model to account for the observed soft X-ray emission. I_{distant} is dominated by the I_{halo} term because $I_{\text{halo}} > I_{\text{extragal}}$ towards high- $|b|$ directions. To separate I_{halo} and I_{extragal} , we would need supplementary *ROSAT* PSPC pointed data (see Barber et al. 1996; Cui et al. 1996; and our discussion in Sect. 5.1). We thus arrive at the simplified radiation-transfer equation

$$I_{\text{SXR}} = I_{\text{LHB}} + I_{\text{distant}} \cdot e^{-\sigma_{\text{distant}} \cdot N_{\text{HI}}(\text{total})} \quad (2)$$

This equation is of the form earlier studied by Marshall & Clark (1984). In the following we show that Eq. (2) represents the observed situation well.

3.4. Evaluation of the radiation-transfer equation

3.4.1. The general approach

We evaluated the SXRb radiation-transfer equation (Eq. 2) using several different methods. Table 1 lists the N_{HI} range for each field. Traced by N_{HI} , we evaluate σ_{distant} and the corresponding attenuation of I_{distant} . A standard method (see e.g. Herbstmeier et al. 1995) involves fitting Eq. (2) to the data, plotted in the form of a scatter diagram of observed SXRb count rate versus total N_{HI} . The disadvantage of such a method is that it neglects the positional information of the data.

An alternative method was introduced by Kerp et al. (1996), who questioned the assumption that all of the H I is located between the observer and the distant X-ray sources; the SXRb/ N_{HI} relation might depend on the kinematic range of integration entering N_{HI} . They evaluated the modelled SXRb intensity distribution according to Eq. (2) for each image pixel. Hence they determined the deviation between the observed and the modelled SXRb intensity distribution, giving a measure of the degree of correlation or anti-correlation of observed and modelled SXRb images. By averaging the individual deviation values of the image pixels across the entire field, they calculated the brightness of the source terms in Eq. (2). The intensities I_{LHB} and I_{distant} were tuned to minimize the difference between both images. This method accounts for the location of the X-ray absorbing clouds within the field and directly reveals the areas where the X-ray data significantly deviate from the modelled mean intensity values.

Here, we optimize the method of Kerp et al. (1996) with respect to evaluation of the derived count rate of the I_{distant} component. We calculated the optimal I_{distant} value using Eq. (2) individually for each image pixel. For instance, if the distant X-ray source is patchy or if the distribution of N_{HI} does not correctly trace the amount of X-ray absorbing matter (perhaps due to neglecting the existence of H_2 and H^+), then a very patchy modelled SXRb intensity pattern would have followed, whereas, in fact, it was determined as quite constant.

3.4.2. First results

Fig. 2 illustrates our results, comparing, for one of our fields, the SXRb distribution observed by the *ROSAT* PSPC with the modelled situation. In order to calculate this modelled map, we determined a constant I_{distant} intensity level across the entire field. In our procedure we let a constant I_{distant} X-ray background intensity penetrate through the absorbing neutral interstellar medium – Fig. 2c shows the N_{HI} distribution as tracing absorption at $|v_{\text{LSR}}| \leq 100 \text{ km s}^{-1}$ – and add the I_{LHB} emission, also assumed to be constant, to this attenuated SXRb map. We tuned both constant X-ray source intensity levels of Eq. (2) in order to obtain the best fit to the observations.

To quantify this result, we tested the hypothesis that the differences between the observed and modelled intensity distributions are statistical deviations and not uncertainties introduced by the modelling of the X-ray data. The observed minus modelled X-ray intensity distribution was binned into a histogram

(100 bins) showing the frequency of the deviation versus the deviation value. The histogram was quantitatively compared with a Gaussian distribution using a χ^2 test. We found $\chi^2 = 67$, well below the acceptable value of $\chi^2 = 120$ for 96 degrees of freedom, and a rejection threshold of 0.05. The hypothesis that both distributions are significantly different has to be rejected. This confirms that our approach of assuming constant I_{LHB} and I_{distant} matches the observed situation well. Additionally, this finding confirms that H I is the best tracer of the photoelectric absorption and that H^+ as well as H_2 influence the soft X-ray radiation transfer on a much lower level compared to H I. Thus, we conclude that I_{distant} can be approximated well by an intensity which is constant across the entire field: the distant soft X-ray background radiation is not patchy on angular scales of some tens of degrees. This finding was verified for all analyzed fields, distributed across the sky. The absolute value of I_{distant} varies significantly, however, between the individual fields. Because I_{extragal} is plausibly constant across the entire sky, the large-scale variation of I_{distant} is entirely attributed to I_{halo} . This will be discussed in detail in Sect. 5.1.

3.4.3. Interpretation of the results

Following the procedures described below, we scaled the intensity of a constant-intensity X-ray background source beyond the entire N_{HI} contribution shown in Fig. 2c. This yielded the image of the modelled SXRb intensity distribution shown in Fig. 2b. In Fig. 2a, we superposed, as contour lines, the deviations between the observed and the modelled SXRb intensity distribution, starting with the $4\text{-}\sigma$ level and increasing in steps of 2σ . Dashed lines indicate areas where the modelled SXRb intensity is too bright, or where we missed additional X-ray absorbers not traced by the H I radiation; solid lines mark areas where *ROSAT* detected more radiation than expected by the H I data. At these positions, we have either overestimated the amount of absorbing matter or we are observing true excess X-ray emission. This excess corresponds to some 25% of the total SXRb intensity. In general, an underestimate of the amount of matter attenuating the X-rays is more likely than an overestimate, because neither H_2 nor H^+ is represented by the 21-cm tracer. Thus, it seems likely that the dashed contours indicate the presence of additional absorbing matter, but that the solid contours indicate X-rays in excess of the average.

3.4.4. Evaluation of I_{distant}

We evaluated the level of the modelled constant distant X-ray source intensity using three additional methods. First, we averaged the X-ray halo intensities across the entire map over areas of equal N_{HI} in bins of $\Delta N_{\text{HI}} = 1 \cdot 10^{19} \text{ cm}^{-2}$. This yielded the dependence of the X-ray halo intensities on the amount of absorbing H I shown in Fig. 3. The slope of the dependence is a function of the assumed I_{LHB} count rate. If the I_{LHB} count rate is underestimated, we obtain a correlation of X-ray halo intensity with N_{HI} ; in case of an overestimate of I_{LHB} , we obtain an anti-correlation. We tuned the I_{LHB} value such that the

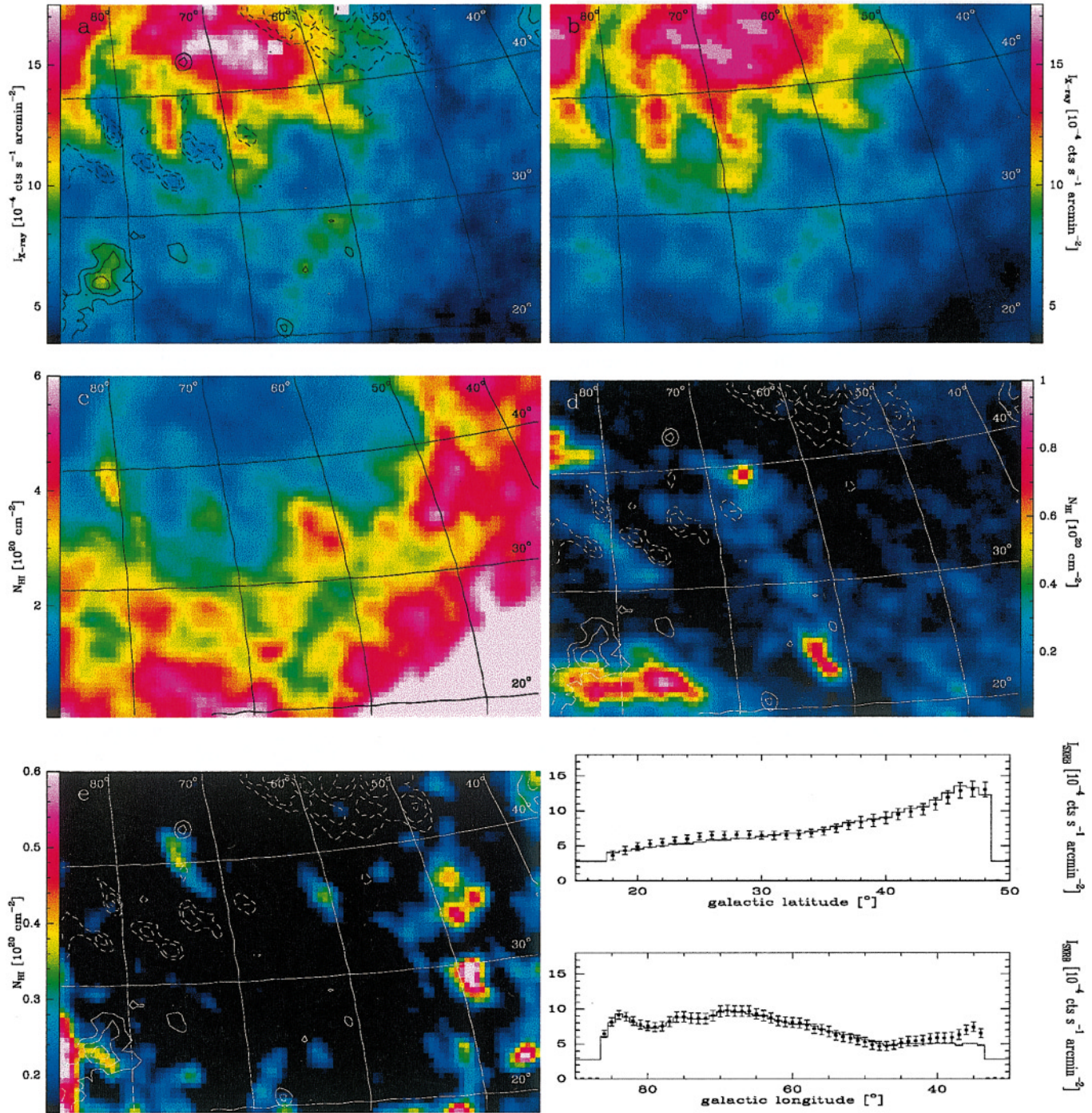


Fig. 2a–f. Caption see page 219

dependence is minimized. This alignment corresponds to the assumption that the $\frac{1}{4}$ keV radiation is independent of the amount of HI along the line of sight. Such is certainly not the case for specific areas of the galactic sky. For example, towards the North Polar Spur (Egger & Aschenbach 1995) the X-ray intensity is *not* distributed independently from the N_{HI} structure.

Second, we averaged both the $\frac{1}{4}$ keV and the N_{HI} data over l and b , respectively, and compared these mean observed intensity values with the model. This method allows searching for

systematic uncertainties introduced by the modelling of the X-ray data. We tested the hypothesis that areas of the sky with the same N_{HI} values correspond to unique I_{distant} and I_{LHB} values, within the uncertainties of the X-ray data. We evaluated the dependence of the source terms in Eq. (2) on the galactic l and b profiles. The derived values for I_{LHB} and I_{distant} agree with those calculated by the first method. Fig. 2f shows the dependence on l and b of the soft X-ray radiation-transfer equation solved with the same intensity values for the LHB and the galac-

Fig. 2a–f. Maps of the part of HVC complex C at both lower l and lower b (see Sect. 4.1.1). **a** Observed $\frac{1}{4}$ keV *ROSAT* PSPC map. Dark colours denote low brightnesses ($I_{1/4\text{keV}}(\text{min}) = 3.5 \cdot 10^{-4} \text{ cts s}^{-1} \text{ arcmin}^{-2}$); bright colours, strong emission ($I_{1/4\text{keV}}(\text{max}) = 17.5 \cdot 10^{-4} \text{ cts s}^{-1} \text{ arcmin}^{-2}$). Solid lines indicate areas where more soft X-ray emission is observed than expected by the model of Eq. (2); dashed lines enclose areas where the X-ray emission is weaker than expected. The lowest contour represents the $4\text{-}\sigma$ level; the contour step is 2σ ($\sigma \approx 0.5 \cdot 10^{-4} \text{ cts s}^{-1} \text{ arcmin}^{-2}$). **b** Modelled situation which results if a constant SXRb, attenuated only by the N_{HI} values (at $|v_{\text{LSR}}| \leq 100 \text{ km s}^{-1}$) shown in panel **c**, with $I_{\text{distant}} = (25 \pm 4) \cdot 10^{-4} \text{ cts s}^{-1} \text{ arcmin}^{-2}$, is combined with the unabsorbed local radiation of $I_{\text{LHB}} = (2.8 \pm 0.5) \cdot 10^{-4} \text{ cts s}^{-1} \text{ arcmin}^{-2}$, also assumed constant across the field. The modelled map has the same maximum and minimum intensity values as the *ROSAT* image shown in panel **a**. All images have the same angular resolution of $48'$. **c** N_{HI} distribution contributed from $|v_{\text{LSR}}| \leq 100 \text{ km s}^{-1}$: $N_{\text{HI}}(\text{min}) = 6 \cdot 10^{19} \text{ cm}^{-2}$, $N_{\text{HI}}(\text{max}) = 6 \cdot 10^{20} \text{ cm}^{-2}$. **d** Greyscale: N_{HI} distribution contributed by HVC velocities, ($-450 \text{ km s}^{-1} \leq v_{\text{LSR}} \leq -100 \text{ km s}^{-1}$): $N_{\text{HI}}(\text{min}) = 1 \cdot 10^{19} \text{ cm}^{-2}$, $N_{\text{HI}}(\text{max}) = 1 \cdot 10^{20} \text{ cm}^{-2}$. The contours are as described in **a**. **e** Greyscale: N_{HI} distribution of the IVC velocity regime, ($-75 \text{ km s}^{-1} \leq v_{\text{LSR}} \leq -25 \text{ km s}^{-1}$): $N_{\text{HI}}(\text{min}) = 1.5 \cdot 10^{19} \text{ cm}^{-2}$, $N_{\text{HI}}(\text{max}) = 6 \cdot 10^{19} \text{ cm}^{-2}$. The contours are as described in **a**. **f** Positional dependence (with galactic latitude [top] and longitude [bottom]) of the averaged modelled and observed SXRb intensity profiles for the lower-longitude end of HVC complex C. The solid lines represent the simulated soft X-ray intensity distribution, modelled as described in the text; the points mark the observed distribution and its corresponding $1\text{-}\sigma$ uncertainties. The agreement of the modelled values with those observed indicates that the soft X-ray background radiation is smoothly distributed across the field, and that H I traces predominately the large-scale photoelectric absorption by the galactic interstellar medium.

tic halo plasma as used to derive panel (b) of Fig. 2. There are no significant large-scale differences between the l and b distributions of the observed SXRb radiation and the modelled X-ray intensity derived from the N_{HI} distribution. This indicates that the distant soft X-ray emission is constant, within the statistical limitations of the X-ray data, across each field.

Third, we averaged observed SXRb count rates with a given N_{HI} in steps of $\Delta N_{\text{HI}} = 1 \cdot 10^{19} \text{ cm}^{-2}$ and plotted a simple scatter diagram of I_{SXRb} versus N_{HI} . This method is sensitive to the choice of the source term parameters in Eq. (2), and would reveal erroneous model parameters.

Thus, we confirmed the validity of the soft X-ray radiation-transfer solution using three independent methods. The second and, even more so, the third, method suffers from neglect of the positional information in the *ROSAT* maps. But they show that the I_{distant} values returned are consistent with those of the first method, which does account for the positional information. This indicates that the I_{distant} source term is, within the statistical limitations of the X-ray data, constant on angular scales of several tens of degrees.

We considered the uncertainties of the individual soft X-ray source terms by varying I_{LHB} or I_{distant} independently in a way that the modelled and observed intensities fit within the statistical uncertainties of the data. Because the quantities are field-averaged, the corresponding uncertainties are low. For the local X-ray emission, $\Delta I_{\text{LHB}} \simeq 0.5 \cdot 10^{-4} \text{ cts s}^{-1} \text{ arcmin}^{-2}$; $\Delta I_{\text{distant}} \simeq 3.0 - 7.0 \cdot 10^{-4} \text{ cts s}^{-1} \text{ arcmin}^{-2}$, depending on the averaged N_{HI} value across the field, and thus typically an order of magnitude higher than the LHB plasma.

3.5. X-ray absorption traced by H I

3.5.1. Velocity information in the H I data

Above, we described our investigation of the I_{LHB} and I_{distant} source terms of Eq. (2). Now, we show how we determined the amount of H I absorbing the soft X-rays. The velocity information contained in the H I data gives an additional free parameter in Eq. (2). We can integrate the H I brightness tem-

peratures over different velocity intervals, introducing a kinematic unravelling which may indicate also a spatial separation. Three separate velocity regimes are commonly, albeit somewhat arbitrarily, distinguished in the literature, namely as low-velocity (LV: $|v_{\text{LSR}}| \leq 25 \text{ km s}^{-1}$), intermediate-velocity (IV: $25 \text{ km s}^{-1} \leq |v_{\text{LSR}}| \leq 90 \text{ km s}^{-1}$), and high-velocity (HV: $|v_{\text{LSR}}| \geq 90 \text{ km s}^{-1}$). The low-velocity regime not only samples all of the higher- $|b|$ H I which belongs to the conventional galactic disk, it includes most of the H I which corresponds to the warm diffuse H I layer (e.g. Dickey & Lockman 1990, also denoted as *warm neutral medium*, WNM) as well. If we integrate the H I spectra over the low-velocity regime, we neglect some 10% of the total amount of H I distributed across the field, although this percentage varies from region to region. In some regions, there is as much emission from H I gas at extreme velocities as from LV matter; towards these lines of sight it is not feasible to evaluate the soft X-ray radiation transfer only with the low-velocity N_{HI} . The Draco cloud (Herbstmeier et al. 1996) is an example of an IVC dominating N_{HI} ; in addition, it contains significant amounts of molecular matter. Finally, HVCs may also absorb the distant SXRb source radiation (see Herbstmeier et al. 1995).

3.5.2. Dependence of I_{distant} and I_{LHB} on the N_{HI} velocity interval

To test whether the choice of N_{HI} velocity interval reveals a kinematic unravelling of the source of the SXRb, we integrated the H I emission separately over the LV range $|v_{\text{LSR}}| \leq 25 \text{ km s}^{-1}$, and over two wider velocity ranges $|v_{\text{LSR}}| \leq 50 \text{ km s}^{-1}$ and $|v_{\text{LSR}}| \leq 100 \text{ km s}^{-1}$. Towards high galactic latitudes the latter range encompasses all interstellar gas except the HVCs. The histograms in Fig. 3 represent $I_{\text{distant}} = (I_{\text{SXRb}} - I_{\text{LHB}}) e^{\sigma_{\text{distant}} \cdot N_{\text{HI}}(\text{total})}$ as a function of N_{HI} . Within the uncertainties of the histogram data points (the error bar in Fig. 3), I_{distant} can be considered a constant across the N_{HI} range of $0.5 \cdot 10^{19} \text{ cm}^{-2}$ to $8.0 \cdot 10^{20} \text{ cm}^{-2}$. The horizontal solid line represents our field-averaged best-fit value of I_{distant} , while the

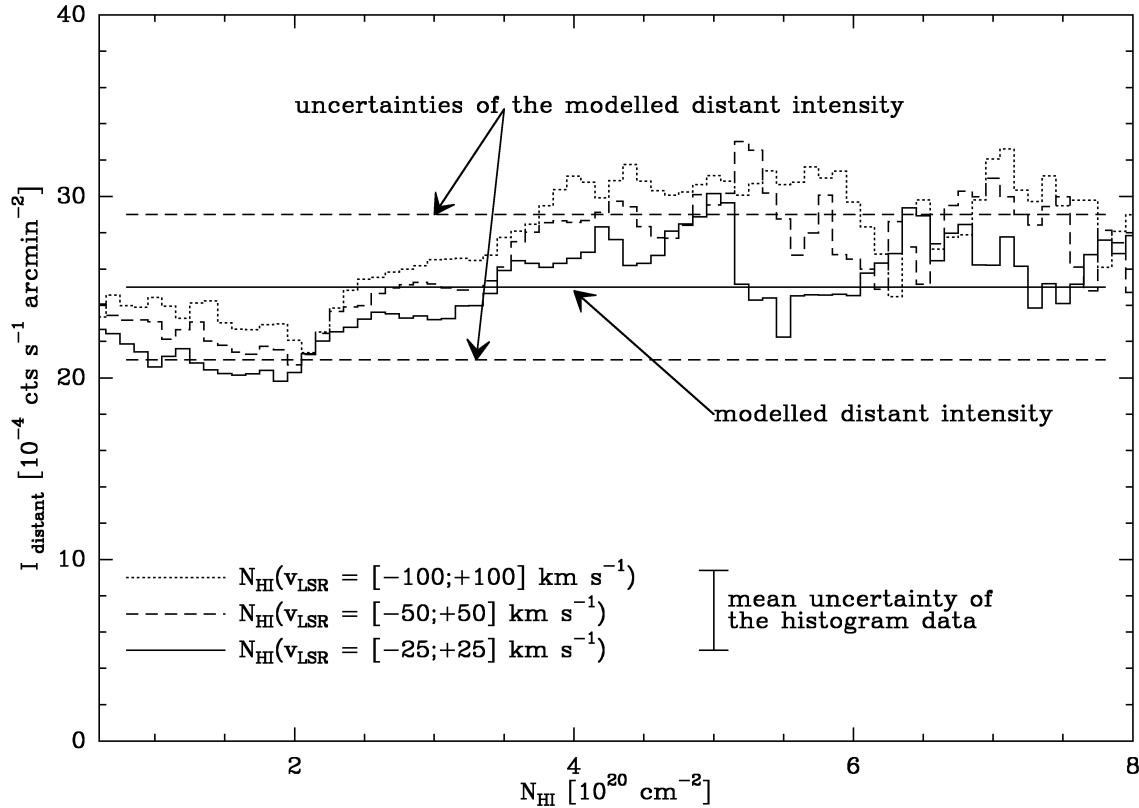


Fig. 3. To constrain the velocity-integration range for N_{HI} , I_{distant} is plotted as a function of N_{HI} for the HVC complex C *ROSAT* data presented in Fig. 2 (see Sect. 4.1.2). The histograms represent I_{distant} versus N_{HI} integrated over three different velocity ranges. The horizontal solid line marks the best-fit I_{distant} intensity level, while the horizontal dashed lines indicate the uncertainty range of the modelled value. Within the uncertainties (the errorbar in the lower-right part of the figure), I_{distant} can be considered as constant across the field of interest. This finding has two major implications; first, I_{LHB} is within the uncertainties also constant across the field of interest. Second, the WNM, already enclosed in the velocity brackets $|v_{\text{LSR}}| \leq 25 \text{ km s}^{-1}$, determines the I_{distant} intensity level. The more extreme velocity ranges introduce only a minor intensity variation, while the functional dependence of I_{distant} on N_{HI} is unaffected.

dashed lines mark the uncertainties of this best-fit value. Taking into account the uncertainties of both, the data and the modelling, the assumption of a constant I_{distant} is justified. With Fig. 3 we can also constrain the expected intensity variation of the I_{LHB} source term, because to evaluate I_{distant} as a function of N_{HI} we *a priori* assumed $I_{\text{LHB}} = \text{const.}$ Consequently, our finding $I_{\text{distant}} = \text{const.}$ implies $I_{\text{LHB}} = \text{const.}$ within the uncertainties of the analysis.

The three histograms in Fig. 3 show that the functional dependence of I_{distant} on N_{HI} is independent of the extent of the velocity range used to evaluate N_{HI} .

However, the mean level of I_{distant} increases proportionally to the extent of the integration range of N_{HI} . Nevertheless, all data points of the three histograms are within the uncertainty range of the modelled I_{distant} intensity level. We conclude that the WNM in the Galaxy determines the mean intensity level of the distant soft X-ray background radiation. Towards high galactic latitudes, the WNM best represents the physical state of the major fraction of the interstellar matter. Accordingly, the H I belonging to the WNM traces the amount of soft X-ray absorbing matter, and determines the mean intensity level of the distant diffuse X-ray radiation. The bulk of the WNM is already

enclosed in the velocity bracket $|v_{\text{LSR}}| \leq 25 \text{ km s}^{-1}$ (Dickey & Lockman 1990). Accordingly, the additional N_{HI} at more extreme velocities increases the mean I_{distant} level, but does not change significantly the functional dependence of I_{distant} on N_{HI} .

The discussion above implies that our modelling of the *ROSAT* X-ray data can be well approximated by constant I_{LHB} and I_{distant} source terms across the extent of the fields of interest (question 1 of Sect. 3). The mean I_{distant} X-ray intensity level is determined by the distribution of the WNM gas. The more extreme velocity ranges represent, on the average, only a minor fraction of the total interstellar gas. Accordingly, the $|v_{\text{LSR}}| \leq 25 \text{ km s}^{-1}$ is sufficient to determine the N_{HI} responsible for the attenuation of the distant diffuse X-ray sources (question 3 of Sect 3). However, our aim is to search for soft X-ray enhancements of HVCs, with respect to the finding shown in Fig. 3 the $|v_{\text{LSR}}| \leq 100 \text{ km s}^{-1}$ yields the highest I_{distant} intensity level. This attributes a maximum of the diffuse X-ray emission to I_{distant} and introduces a systematic bias in our analysis for the *non-detection* of excess X-ray emission associated with HVCs.

4. Individual HVC complexes

To investigate whether soft X-ray enhancements are associated with HVCs, we *excluded* the HVC velocity regime from the velocity range used to determine the absorbing N_{HI} , in particular we integrated N_{HI} over $|v_{\text{LSR}}| \leq 100 \text{ km s}^{-1}$. This exclusion introduces the brightest modelled SXRb intensity just at the positions of the HVCs and thus biases our analysis against detection of soft X-ray enhancements with HVCs, because we evaluate observed minus modelled X-ray intensity distribution only. We now evaluate the solutions of Eq. (2) with N_{HI} determined over the more extreme velocity interval $|v_{\text{LSR}}| \leq 100 \text{ km s}^{-1}$, searching for soft X-ray correlations or anti-correlations with HVCs.

4.1. The HVC complex C

4.1.1. Complex C at lower l and b , and parts of complex D

Kerp et al. (1996) investigated the X-ray intensity distribution towards complex C at $34^\circ \leq l \leq 86^\circ$, $33^\circ \leq b \leq 79^\circ$. Here, we discuss parts of complex C, weaker in HI emission, at lower b . Fig. 2a shows the *ROSAT* PSPC data from the lower- b part of complex C. Panel (b) shows the modelled SXRb intensity distribution, assuming a constant SXRb source intensity across the field. We derived the intensity of the LHB, $I_{\text{LHB}} = (2.8 \pm 0.5) \cdot 10^{-4} \text{ cts s}^{-1} \text{ arcmin}^{-2}$, and of the distant X-ray source, $I_{\text{distant}} = (25 \pm 4) \cdot 10^{-4} \text{ cts s}^{-1} \text{ arcmin}^{-2}$. Both X-ray images in Fig. 2a and b are scaled similarly. A statistical evaluation of the similarity between the observed and modelled X-ray map gives $\chi^2 = 67 < \chi^2_{0.05} = 120$. This confirms that also statistically the observed and modelled X-ray intensity distributions match. In Fig. 2a we superposed, as contours, the deviations between the observed and the modelled SXRb distributions, starting with the $4\text{-}\sigma$ contour level. Dashed contours indicate where the modelled SXRb intensity is brighter than observed; solid contours enclose regions where the modelled SXRb intensity is weaker than observed.

The dashed contours do not enclose the positions of individual HVCs (see Fig. 2d), indicating that we do not detect soft X-ray shadows of HVCs at this significance level. It is more likely that these dashed contour lines of X-ray shadows indicate cloud structure within the LHB. As mentioned in Sect. 3.3.1, the effective photoelectric absorption cross section of the LHB plasma is the largest of all three cross sections: an HI cloud within the LHB will cause a deeper soft X-ray shadow than when the same cloud were located outside the LHB. In consequence, if predicted soft X-ray emission is weaker than observed, one first has to check for the existence of a cloud within the LHB. The dashed contours in Fig. 2a show a patchy distribution; a large area of weaker X-ray emission is located at $l = 70^\circ - 85^\circ$, $b \geq 30^\circ$. Located close to the dashed contours is an elongated HI filament, part of a much more extended local HI structure (Wennmacher et al. 1998, Kerp & Pietz 1998). An N_{HI} maximum of this structure associated with a filament, denoted as LVC 88+36–2, was studied by Wennmacher et al. (1992). Kerp et al. (1993) detected a strong soft X-ray absorption feature as-

sociated with LVC 88+36–2 in pointed *ROSAT* PSPC data and confirmed that the filament is embedded within the LHB. Thus, the dashed contours indicate, most likely, local N_{HI} maxima of an extended HI structure within the LHB (see Kerp & Pietz 1998).

A second region of low observed SXRb emission, at $l = 45^\circ - 65^\circ$ and $b \geq 40^\circ$, is not associated with a previously identified local HI structure. As mentioned in Sect. 3.4.3, an underestimate on the amount of X-ray absorbing matter is more likely than an overestimate, because HI emission traces neither molecular nor ionized gas. The dashed contours may indicate an additional absorber, either located outside of the LHB (and thus only attenuating the I_{distant} term) or within the local bubble. In the former case, we miss $\Delta N_{\text{HI}} \simeq 4 \cdot 10^{20} \text{ cm}^{-2}$ as an absorber; in the latter case, $\Delta N_{\text{HI}} \simeq 1 \cdot 10^{20} \text{ cm}^{-2}$. This difference in absorbing N_{HI} between both model assumptions follows from different amplitudes of the near and distant photoelectric absorption cross sections (see Fig. 1). Consequently, the SXRb minimum is more likely due to a local cloud than to a cloud of higher N_{HI} beyond the local bubble. Hartmann et al. (1998) detected no molecular gas in this direction, although such gas might be anticipated for a cloud outside of the LHB with such a high HI density. A further investigation of the Leiden/Dwingeloo data reveals an HI minimum at $v_{\text{LSR}} \approx -2 \text{ km s}^{-1}$, suggesting that some of the local HI may have been ionized and not quantitatively traced by the distribution of N_{HI} . The distance to the absorber thus remains uncertain.

The solid contours in Fig. 2d enclose an HVC catalogued as #182 by Wakker & van Woerden (1991), at $v_{\text{LSR}} = -190 \text{ km s}^{-1}$, and attributed to HVC complex D. Our analysis suggests an excess soft X-ray emission with a significance level greater than 4σ . The solid contours also enclose nearby regions of intermediate-velocity gas ($-75 \text{ km s}^{-1} \leq v_{\text{LSR}} \leq -25 \text{ km s}^{-1}$, Fig. 2e), implying that IVCs may also be associated with the enhanced X-ray emission. In this particular case, where both HVC and IVC gas appear along the same lines of sight, we cannot determine whether the HVCs or the IVCs are the sources of the excess soft X-ray emission.

Finally, we analyzed the variation of the modelled (Fig. 2b) and observed (Fig. 2a) SXRb emission, as averaged over l and b . We solved the radiation-transfer equation independently for these averaged distributions. Fig. 2f shows the observed and modelled SXRb intensity profiles averaged in l and b . The modelled SXRb intensity profile (solid line) fits the *ROSAT* observation (dots) well. This shows that the dominant part of the soft X-ray attenuation is traced by HI, and that small-scale (0.8°) as well as large-scale ($\sim 30^\circ$) intensity variations of the SXRb can be explained by photoelectric absorption. This result justifies again our assumption that $I_{\text{LHB}} = \text{const.}$ and $I_{\text{distant}} = \text{const.}$ (see Sect. 3.3) across each field.

4.1.2. Complex C at higher l and b

Fig. 4a shows the *ROSAT* $\frac{1}{4}$ keV map of complex C between $99^\circ \leq l \leq 166^\circ$, $12^\circ \leq b \leq 74^\circ$. The field also includes much of HVC complex A as well as the high-velocity filament

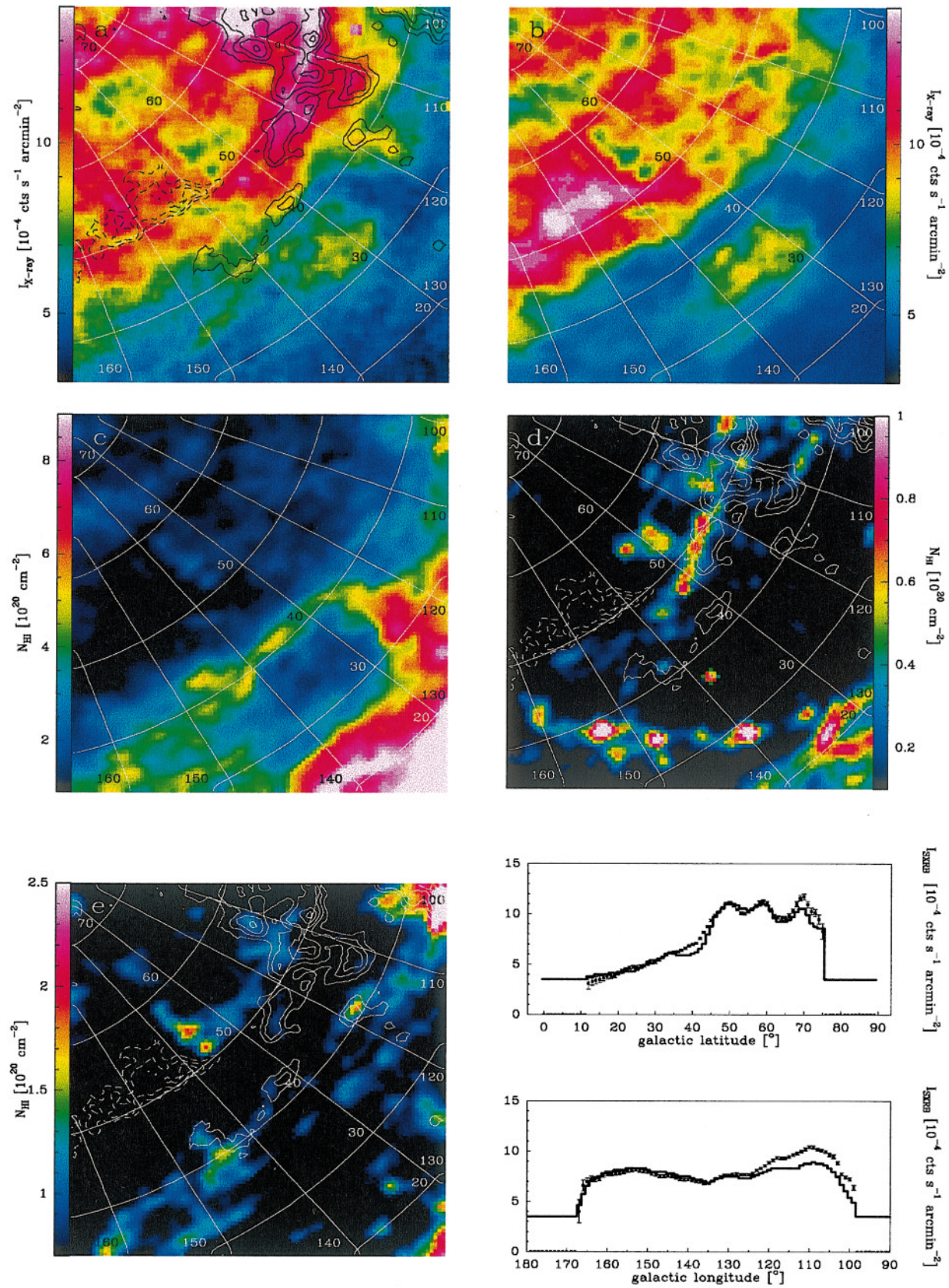


Fig. 4a–f. Caption see page 223

Fig. 4a–f. Soft X-ray background towards the higher- l and $-b$ end of HVC complex C, (see Sect. 4.1.2). **a** The SXRBR intensities observed in the *ROSAT* $\frac{1}{4}$ keV band. **b** The SXRBR map modelled according to Eq. (2) using Leiden/Dwingeloo data and assuming $I_{\text{distant}} = \text{const.} = (16 \pm 3) \cdot 10^{-4} \text{ cts s}^{-1} \text{ arcmin}^{-2}$ in addition to the local X-ray radiation of $I_{\text{LHB}} = (3.5 \pm 0.5) \cdot 10^{-4} \text{ cts s}^{-1} \text{ arcmin}^{-2}$, also assumed constant across the field. Dark colours denote low X-ray intensities ($I_{1/4 \text{ keV}}(\text{min}) = 3.0 \cdot 10^{-4} \text{ cts s}^{-1} \text{ arcmin}^{-2}$); bright colours denote high intensities ($I_{1/4 \text{ keV}}(\text{max}) = 14.0 \cdot 10^{-4} \text{ cts s}^{-1} \text{ arcmin}^{-2}$). **c** The N_{HI} distribution ($9 \cdot 10^{19} \text{ cm}^{-2} \leq N_{\text{HI}} \leq 9 \cdot 10^{20} \text{ cm}^{-2}$) across the field within the range $|v_{\text{LSR}}| \leq 100 \text{ km s}^{-1}$. **d** Greyscale: the N_{HI} distribution ($1 \cdot 10^{19} \text{ cm}^{-2} \leq N_{\text{HI}} \leq 1 \cdot 10^{20} \text{ cm}^{-2}$) in the HVC regime, $-450 \text{ km s}^{-1} \leq v_{\text{LSR}} \leq -100 \text{ km s}^{-1}$. The contours are described below. **e** Greyscale: the N_{HI} distribution ($7 \cdot 10^{19} \text{ cm}^{-2} \leq N_{\text{HI}} \leq 2.5 \cdot 10^{20} \text{ cm}^{-2}$) in the IVC regime, $-75 \text{ km s}^{-1} \leq v_{\text{LSR}} \leq -25 \text{ km s}^{-1}$. The contours are described below. **f** The intensity profiles averaged in l and b from the maps in panel **a**, dots with error-bars, and **b**, solid lines. Superposed as contours are the intensity deviations between the observed **a** and modelled **b** SXRBR maps. The contours proceed from the $5\text{-}\sigma$ level in steps of 2σ ($\sigma \approx 0.65 \cdot 10^{-4} \text{ cts s}^{-1} \text{ arcmin}^{-2}$). Solid contours in **a**, **d**, and **e** mark areas of excess X-ray emission; dashed contours mark areas of weaker X-ray emission than expected from the map in **b**. The angular resolution of the images is $48'$.

which connects HVC complex C with A (Wakker & van Woerden 1991). The map covers such a large range in l ($\simeq 67^\circ$) and b ($\simeq 62^\circ$) that the N_{HI} distribution varies appreciably across the field. This yields the opportunity to study the variation of the SXRBR source intensity distribution with galactic latitude. In the upper left of Fig. 4a, strong soft X-ray attenuation by the neutral matter associated with the North Celestial Pole Loop (Meyerdierks et al. 1991) is visible (see also Fig. 4c, $l \sim 135^\circ$, $b \sim 35^\circ$). Significant amounts of molecular material are found near this structure (Heithausen et al. 1993), for instance in the Polaris Flare ($l \sim 125^\circ$, $b \sim 30^\circ$; Heithausen & Thaddeus 1990). Towards the Polaris Flare, the Leiden/Dwingeloo data show a maximum of $N_{\text{HI}} \simeq 9 \cdot 10^{20} \text{ cm}^{-2}$ (Fig. 4c). The Lockman et al. (1986) area of minimum N_{HI} ($l \sim 152^\circ$, $b \sim 52^\circ$) is located at the other end of the field. The data show a ratio $N_{\text{HI max}}/N_{\text{HI min}} = 25$ in the absorbing column densities.

We evaluated the X-ray source terms using all three methods described in Sect. 3.4.4 and found $I_{\text{LHB}} = (3.5 \pm 0.5) \cdot 10^{-4} \text{ cts s}^{-1} \text{ arcmin}^{-2}$ and $I_{\text{distant}} = (16 \pm 3) \cdot 10^{-4} \text{ cts s}^{-1} \text{ arcmin}^{-2}$. The χ^2 -test of the observed and modelled X-ray map indicates that $\chi^2 = 170 > \chi^2_{0.05} = 120$. The differences between the observed and modelled map are significant. Most probably, the structure of the interstellar medium covered by the field of interest is much too inhomogeneous to be fitted by our simple approach. However, Fig. 4f shows that the modelling of the X-ray data fits the overall SXRBR intensity distribution well, especially if we take the bright X-ray enhancements around $b \sim 50^\circ$ into consideration. However, to distinguish between excess emission areas and large scale intensity variations of I_{LHB} and I_{distant} , we restrict our interpretation of the X-ray deviations to high galactic latitudes ($b \geq 35^\circ$) and to peak deviations more significant than 5σ . In Fig. 4a, most of the contours are oriented parallel to $b \sim 50^\circ$. Nearby are the main parts of HVC complex C (see Fig. 4d) and the Lockman et al. window, which is enclosed by dashed contours. In this region, our I_{LHB} value is lower by a factor of two than the value given by Snowden et al. (1994b, 1998), while I_{distant} is higher by about the same factor. To investigate this discrepancy (see Freyberg 1997), we extracted the Lockman Window data from our map and evaluated the radiation transfer equation in this area once again, restricting our analysis to a region of 12° in extent in both l and b . We derived $I'_{\text{LHB}} = (6.0 \pm 0.5) \cdot 10^{-4} \text{ cts s}^{-1} \text{ arcmin}^{-2}$

and $I'_{\text{distant}} = (7 \pm 3) \cdot 10^{-4} \text{ cts s}^{-1} \text{ arcmin}^{-2}$, applying only the first method described in Sect. 3.4.4. Using the second and third methods, we find values which, although in closer agreement with Snowden et al. (1994b), do not fit the averaged l and b intensity profiles. Moreover, if we extrapolate the $I'_{\text{LHB/distant}}$ values to the data shown in Fig. 4a, we fail to reproduce the observations. In contrast, the first-method values ($I_{\text{LHB/distant}}$) do fit the Lockman Window region in the averaged l and b profiles (see Fig. 4f). This shows that a solution of the radiation-transfer equation demands determination of I_{distant} over areas large enough not to be biased by local events.

The solid contours roughly trace some of the brighter parts of HVC complex C, suggesting that these bright HVCs, in addition to other parts of complex C (Kerp et al. 1996), are associated with excess soft X-ray emission. The Pietz et al. (1996) H I “velocity-bridges” suggest the interaction of some HVC matter with the conventional-velocity regime. The velocity bridges VB 112 + 48 and VB 115 + 47, both at the high- b end of complex C, are enclosed by $5\text{-}\sigma$ contours. VB 112 + 57.5 is an area of soft X-ray radiation enhanced to the $11\text{-}\sigma$ level. VB 111 + 35 and VB 133 + 55 were not detected as enhancements in the $\frac{1}{4}$ keV *ROSAT* data. If we add the four velocity bridges already found to be X-ray bright by Kerp et al. (1996) using similar methods, we find that 7 of 11 bridges are located close to soft X-ray enhancements. The velocity bridges span the range of conventional velocities to those of the HVCs, and thus their association with enhanced X-ray emission does not, in itself, distinguish between an HVC or an IVC connection (see Fig. 4e, and Sect. 5.2).

The suggestion that velocity bridges are associated with a distortion of the velocity field due to an HVC, requires disproving that the bridges are different from normal IVC structures. The large distance to the HVCs (several kpc for the nearest, Wakker & van Woerden 1997, and possibly hundreds of kpc for many HVCs, Blitz et al. 1998) make it unlikely that HVCs are physically linked to those IVCs which are carriers of dust. Much of the intermediate-velocity H I is associated with dust cirri (Deul & Burton 1990), and is therefore likely to be rather local, rarely extending to z -heights of more than 150 pc. The velocity regime of cirrus-carrying IVCs, however, is frequently trespassed upon by HVCs: the crossing of the Magellanic Stream from positive to negative velocities is a case in point. HVC gas trespassing on lower velocities will have a dif-

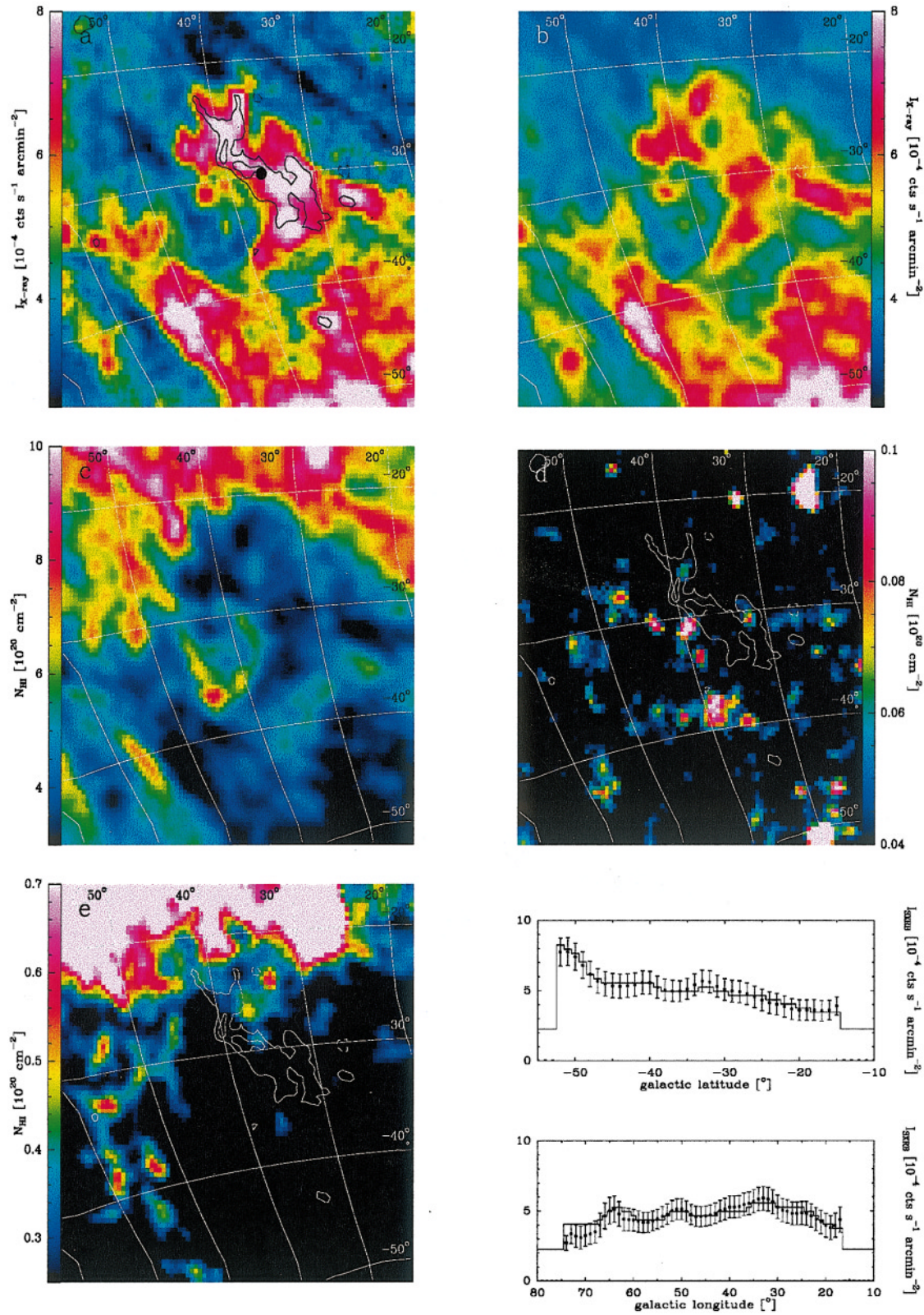


Fig. 5a–f. Caption see page 225

Fig. 5a–f. Maps of the X-ray and H I sky towards HVC complex GCN (see Sect. 4.2). **a** *ROSAT* $\frac{1}{4}$ keV SXR distribution ($I_{1/4 \text{ keV}}(\text{min}) = 2.5 \cdot 10^{-4} \text{ cts s}^{-1} \text{ arcmin}^{-2}$ and $I_{1/4 \text{ keV}}(\text{max}) = 8 \cdot 10^{-4} \text{ cts s}^{-1} \text{ arcmin}^{-2}$). **b** Modelled SXR image derived from the H I data, assuming both a constant distant X-ray background $I_{\text{distant}} = (30 \pm 7) \cdot 10^{-4} \text{ cts s}^{-1} \text{ arcmin}^{-2}$ and a constant local X-ray source $I_{\text{LHB}} = (2.3 \pm 0.5) \cdot 10^{-4} \text{ cts s}^{-1} \text{ arcmin}^{-2}$. Solid contours indicate excess X-ray emission; dashed contours indicate an emission deficiency. The contours proceed from the $4\text{-}\sigma$ level in $2\text{-}\sigma$ steps ($\sigma \approx 0.8 \cdot 10^{-4} \text{ cts s}^{-1} \text{ arcmin}^{-2}$). **c** N_{HI} distribution of the soft X-ray absorbing ISM ($|v_{\text{LSR}}| \leq 100 \text{ km s}^{-1}$ colour coded within the range $3 \cdot 10^{20} \text{ cm}^{-2} \leq N_{\text{HI}} \leq 1 \cdot 10^{21} \text{ cm}^{-2}$). **d** Greyscale: the HVC N_{HI} distribution ($-450 \text{ km s}^{-1} \leq v_{\text{LSR}} \leq -100 \text{ km s}^{-1}$ and $4 \cdot 10^{18} \text{ cm}^{-2} \leq N_{\text{HI}} \leq 1 \cdot 10^{19} \text{ cm}^{-2}$). The contours are described in **b**. **e** IVC N_{HI} distribution ($25 \text{ km s}^{-1} \leq |v_{\text{LSR}}| \leq 75 \text{ km s}^{-1}$ and $2.5 \cdot 10^{19} \text{ cm}^{-2} \leq N_{\text{HI}} \leq 7.0 \cdot 10^{19} \text{ cm}^{-2}$). The contours are described in **b**. **f** SXR intensity profiles, averaged in l and b across the map (panel **a**: dots and error bars; panel **b**: solid lines). The images in **a** and **b** are scaled identically and have an angular resolution of $48'$. The dot in **a** marks the position of Mrk 509 where Sembach et al. (1995) detected highly-ionized high-velocity gas in HST absorption-line measurements, at a location coinciding with excess soft X-ray emission.

ferent chemical composition from the dust-carrying IVCs. In Sect. 5.2 we will discuss this point for HVC complex C in more detail.

In the special case of a wide extent in galactic latitude, it is interesting to study the observed and modelled SXR intensity variations against l and b , as shown in Fig. 4f. Again, the solid line marks the modelled intensity profile based only on H I data. The b -variations show quantitative agreement between observation and modelled values, deviating only close to $b \simeq 40^\circ$, at the location of the North Celestial Pole Loop (region of highest opacity), and above $b \geq 65^\circ$. These deviations are significant: the error-bars correspond to the $3\text{-}\sigma$ level. Most likely, we observe an intensity variation of I_{LHB} proportional to increasing b . Fig. 4f shows that the X-ray intensity variation is correctly predicted by the modelled SXR intensity distribution, but starting at $b \geq 65^\circ$, the modelled SXR intensity deviates increasingly from the observed one. Towards these high- b regions we may predominantly observe the local interstellar medium, and consequently a larger extent of the local X-ray emitting region. Finally, we note that the modelled SXR longitude profile closely matches the observed one for $l \gtrsim 130^\circ$. This position coincides with the border of the X-ray enhancements associated with HVC complex C.

4.2. The HVC complex GCN

The mean N_{HI} towards the galactic center HVC complex GCN ($18^\circ \leq l \leq 73^\circ$, $-52^\circ \leq b \leq -15^\circ$) is significantly higher than towards the other regions discussed here. The field displays the complex H I column density structure within the range $|v_{\text{LSR}}| \leq 100 \text{ km s}^{-1}$ (Fig. 5c). Solving of the radiation-transfer equation gives $I_{\text{LHB}} = (2.3 \pm 0.5) \cdot 10^{-4} \text{ cts s}^{-1} \text{ arcmin}^{-2}$ and $I_{\text{distant}} = (30 \pm 7) \cdot 10^{-4} \text{ cts s}^{-1} \text{ arcmin}^{-2}$. The χ^2 test of the observed and modelled data gives $\chi^2 = 59 < \chi^2_{0.05} = 120$. Fig. 5 shows the *ROSAT* data (panel a) our solution of Eq. (2) (panel b) using the Leiden/Dwingeloo H I data. This field shows well-defined large-scale X-ray intensity gradients in the *ROSAT* data which are reproduced by our solution of Eq. (2), confirming that the intensity variations are dominated by photoelectric absorption effects.

The distant X-ray intensity (I_{distant}) is quite high, and (within the uncertainties) equal to the intensity value of the lower end of HVC complex C (Sect. 4.1.1). Furthermore, the

I_{LHB} intensity of both areas agree. We note that both *ROSAT* areas cover a comparable range in galactic coordinates, but refer to opposite galactic hemispheres, which suggests that closer to the inner Galaxy, the northern and southern galactic sky have approximately the same SXR distant source intensity, and that I_{distant} is not patchy across the individual fields. Thus, we can consider I_{distant} as constant towards the same galactic longitude range in both galactic hemispheres.

The bright X-ray area, located near in the center of Fig. 5a, shows excess soft X-ray emission enclosed by solid contours. The galaxy Mrk 509 is marked by the dot. Sembach et al. (1995) used HST absorption-line measurements to detect highly-ionized high-velocity gas belonging to HVC complex GCN. They attribute the source of the ionization to photoionization. Our *ROSAT* data suggest, additionally, the presence of collisionally ionized gas along the line of sight towards Mrk 509. Sembach et al. may have detected the cooler portion of the collisionally ionized plasma. Figure 5d shows the distribution of the GCN clouds across the field. They are patchily distributed and have only low column densities of $N_{\text{HI}} \simeq 5 \cdot 10^{18} \text{ cm}^{-2}$. Very close by, some filaments are found which belong to the HVC complex GCP; we can not distinguish whether the excess emission originates in GCN or in GCP. Following Sembach et al. (1995), we attribute the excess emission to complex GCN. Thus, in contrast to HVC complex C, where we found a close positional correlation between neutral HVC gas and the X-ray bright areas, the GCN complex allows no straightforward interpretation. Blitz et al. (1998) include complex GCN amongst those suggested to be at large, extragalactic distances. If this is true, one must consider the physical circumstances which would allow the presence of collisionally- and photoionized gas associated with this complex.

Fig. 5f shows the l and b profiles of the GCN maps. Again, the modelled SXR intensity distribution fits the observation, confirming that the areas of excess soft X-ray radiation are well determined by the methods applied.

4.3. The HVC complex WA

HVC complex WA (Wannier et al. 1972; see also Wakker & van Woerden 1991), roughly confined to the region $218^\circ \leq l \leq 270^\circ$, $24^\circ \leq b \leq 52^\circ$, displays the positive velocities ($v_{\text{LSR}} \sim +150 \text{ km s}^{-1}$) characteristic of most HVCs in this

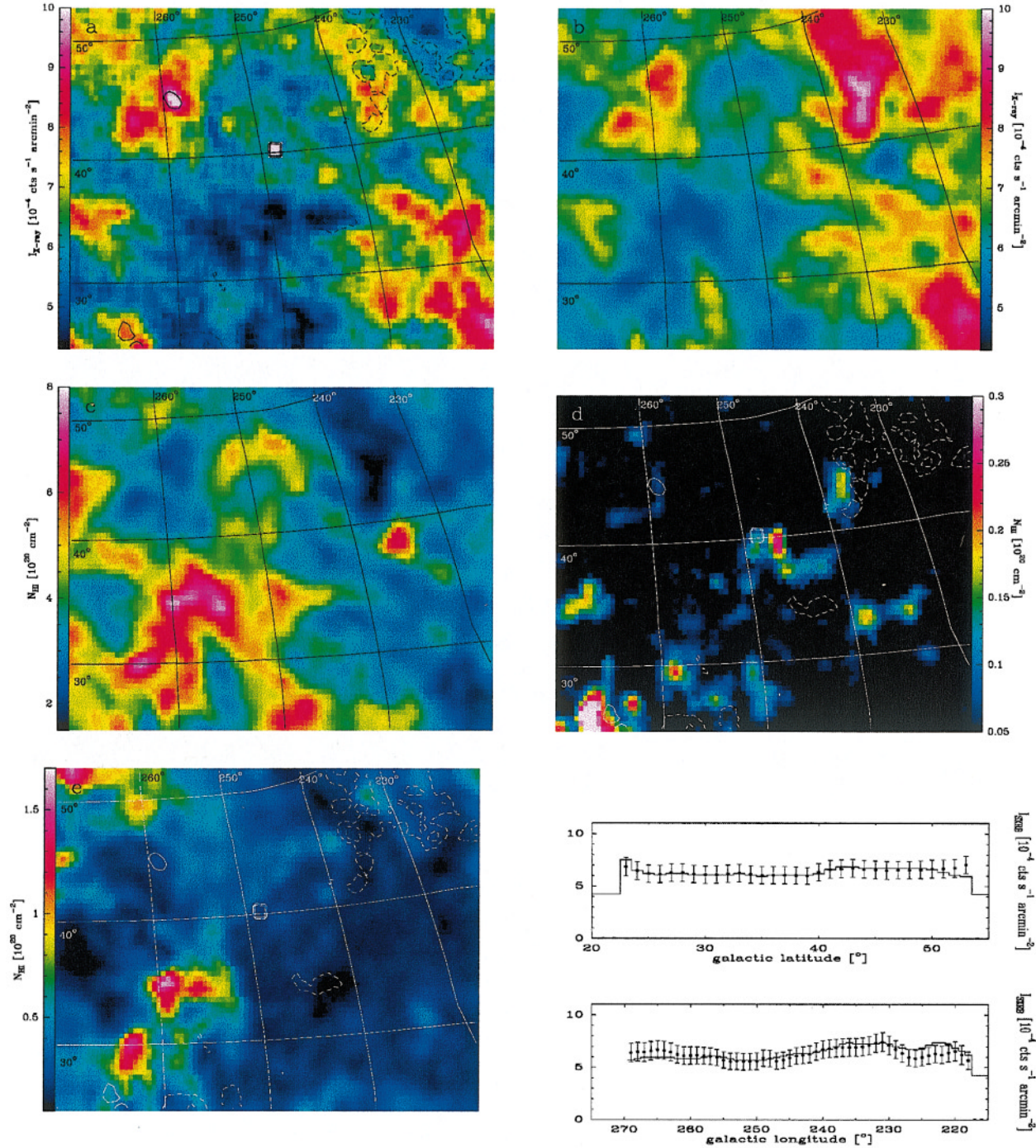


Fig. 6a–f. Maps of the X-ray and H I sky towards HVC complex WA (see Sect. 4.3). **a** Observed $1/4$ keV SXR distribution ($I_{1/4 \text{ keV}}(\text{min}) = 4.3 \cdot 10^{-4} \text{ cts s}^{-1} \text{ arcmin}^{-2}$ and $I_{1/4 \text{ keV}}(\text{max}) = 10 \cdot 10^{-4} \text{ cts s}^{-1} \text{ arcmin}^{-2}$). **b** Modelled SXR image derived from the H I data, assuming a constant intensity distribution across the field of both X-ray source terms, $I_{\text{distant}} = (13 \pm 4) \cdot 10^{-4} \text{ cts s}^{-1} \text{ arcmin}^{-2}$ and $I_{\text{LHB}} = (4.3 \pm 0.5) \cdot 10^{-4} \text{ cts s}^{-1} \text{ arcmin}^{-2}$. Images **a** and **b** are scaled identically; the angular resolution of the maps is $48'$. Solid contours indicate excess X-ray emission; dashed contours, a lack of emission. The contours proceed from the $4\text{-}\sigma$ level in steps of 2σ , where $\sigma \approx 0.8 \cdot 10^{-4} \text{ cts s}^{-1} \text{ arcmin}^{-2}$. **c** Distribution of N_{HI} in the range $|v_{\text{LSR}}| \leq 100 \text{ km s}^{-1}$ with $1.5 \cdot 10^{20} \text{ cm}^{-2} \leq N_{\text{HI}} \leq 8 \cdot 10^{20} \text{ cm}^{-2}$. **d** Greyscale: the distribution of N_{HI} in the appropriate positive-velocity HVC range ($100 \text{ km s}^{-1} \leq v_{\text{LSR}} \leq 400 \text{ km s}^{-1}$ with $5 \cdot 10^{18} \text{ cm}^{-2} \leq N_{\text{HI}} \leq 3 \cdot 10^{19} \text{ cm}^{-2}$). The contours are described in **b**. **e** Greyscale: the distribution of N_{HI} in the IVC range ($25 \text{ km s}^{-1} \leq v_{\text{LSR}} \leq 75 \text{ km s}^{-1}$ with $1 \cdot 10^{19} \text{ cm}^{-2} \leq N_{\text{HI}} \leq 1.7 \cdot 10^{20} \text{ cm}^{-2}$). The contours are described in **b**. **f** SXR intensity averaged over l and b . The dots and error bars refer to the observed data in **a**; the solid line represents the model in **b**.

general region of the sky. The radial velocity is, of course, only one component of the velocity vector; the positive radial velocity does not rule out, by itself, that the HVC could be colliding with the galactic disk. Regarding the X-ray radiation transfer, it is interesting that the HVC complex WA is located opposite the direction of HVC complex C, but also in the northern sky.

Fig. 6 shows the *ROSAT* $\frac{1}{4}$ keV map (panel a) and the modelled SXR intensity (panel b). We derive an intensity of $I_{\text{LHB}} = (4.3 \pm 0.5) \cdot 10^{-4} \text{ cts s}^{-1} \text{ arcmin}^{-2}$ for the LHB, and $I_{\text{distant}} = (13 \pm 4) \cdot 10^{-4} \text{ cts s}^{-1} \text{ arcmin}^{-2}$ for the distant X-rays. These LHB and distant X-ray count rates mark the extreme intensity values found in our sample of HVC complexes. Because of the short *ROSAT* integration times towards complex WA, the observed and modelled SXR maps show some deviations. The χ^2 -test of the maps reveal that $\chi^2 = 34 < \chi^2_{0.05} = 120$. Statistically, the modelled SXR map fits the observed one well. However, only a few $4\text{-}\sigma$ contours are present in Fig. 6a.

The SXR radiation is locally weaker near $l \sim 230^\circ$, $b \sim 48^\circ$ (4σ). Either we miss additional matter attenuating the soft X-rays but not traced by N_{HI} , or, more likely, the photoelectric absorption cross section is locally larger due to a cloud within the LHB plasma. At $v_{\text{LSR}} \approx 0 \text{ km s}^{-1}$, HI maps in the Leiden/Dwingeloo atlas show a local deficiency of neutral gas, correlated with the contours given in Fig. 6.

Toward the general direction of HVC complex WA we identified soft X-ray enhancements with known HVCs (Fig. 6d). The $4\text{-}\sigma$ contour centered $l = 258^\circ$, $b = 45^\circ$ is positionally associated with the HVC catalogued as #66 by Wakker & van Woerden (1991). The solid contour near $l = 264.8^\circ$, $b = 26.5^\circ$, lies in between the HVCs catalogued as #176 and #162. (These HVCs are within our WA field but Wakker & van Woerden (1991) did not assign them to complex WA.) Because of the limited quality of the *ROSAT* data and the possibility of residual systematic uncertainties, we do not claim a firm detection of excess X-ray emission from the WA HVCs. Fig. 6d shows the N_{HI} distribution of the HVCs towards the field. The N_{HI} range of the HVCs displayed is only $5 \cdot 10^{18} \text{ cm}^{-2} \leq N_{\text{HI}} \leq 3 \cdot 10^{19} \text{ cm}^{-2}$. Fig. 6f shows the averaged SXR intensity profiles derived from the observed and modelled $\frac{1}{4}$ keV SXR data; within the uncertainties of the data, the modelled SXR variation fits the observational data well.

5. Discussion

5.1. The radiation transfer of $\frac{1}{4}$ keV photons

We discuss here the accuracy of our solution of the radiation transfer in confirming the detections of enhanced soft X-ray radiation close to HVCs, and some general properties of the distant soft X-ray sources. The compelling similarity between the observed and the modelled SXR intensity distributions, based only on HI data, supports several conclusions. It argues for a smooth intensity distribution of the SXR sources, at greater distances than the galactic HI. Moreover, the smoothness of the SXR source distribution is emphasized by the success of a constant intensity background distribution in fitting the *ROSAT*

Table 2. Summary of the derived $\frac{1}{4}$ keV X-ray intensities, in units of $10^{-4} \text{ cts s}^{-1} \text{ arcmin}^{-2}$. The HVC complexes investigated by Herbstmeier et al. (1995) and by Kerp et al. (1996) are indicated by asterisks. The fields are ordered according to the angular distance of each map center from the galactic center (see Fig. 7). The righthand column gives the χ^2 value of the difference between the modelled and observed X-ray map. Using a significance level of 0.05 the acceptable χ^2 is 120 with 96 degrees of freedom.

complex	l_c	b_c	I_{LHB}	I_{distant}	χ^2
GCN	40°	-32°	2.3 ± 0.5	30 ± 7	59
C low, D	63°	$+32^\circ$	2.8 ± 0.5	25 ± 4	67
C*	94°	$+51^\circ$	4.4 ± 1.0	18 ± 3	71
WA	247°	$+38^\circ$	4.3 ± 0.5	13 ± 4	34
C high	132°	$+43^\circ$	3.5 ± 0.5	16 ± 3	170
M*	170°	$+60^\circ$	~ 6.5	≤ 10	

data well across several tens of degrees as suggested by Pietz et al. (1998b). This situation does not rule out that there may be large-scale intensity gradients across the entire galactic sky. Also, the averaged variations plotted against galactic l and b do not suggest that, there are no intensity gradients in the SXR, but they do indicate that within the fields considered, the distant X-ray sources do not show significant intensity variations.

Table 2 summarizes the derived intensities of the I_{LHB} and the distant X-ray component, I_{distant} , in order of increasing angular distance of the map center from the galactic center. The variation of the galactic halo intensity noted in Table 2 and plotted in Fig. 7 suggests that towards the inner Galaxy the distant soft X-ray source reaches a local maximum. Because we avoid the area of the North Polar Spur (Egger & Aschenbach 1995), this variation is probably due to the distant SXR source component. Moreover, the distant SXR source intensities tend to decrease in the direction away from the galactic center (see Fig. 7 and the discussion below). This variation with l implies that we indeed observe galactic soft X-ray emission, confirming the findings of Pietz et al. (1998a; 1998b).

A similar intensity variation of the galactic X-ray halo component with b cannot be claimed from our data because all the X-ray maps analyzed are at roughly the same latitude, near $|b| \sim 35^\circ$. Our data suggest, however, that the derived galactic X-ray halo intensity shows the same brightness in the northern and southern sky (Pietz et al. 1998b; Wang 1998). We note further that the derived LHB intensities are proportional to the extent of the local cavity and in agreement with the shape of the LHB derived from absorption-line measurements (e.g. Egger et al. 1996).

The variations of the observed SXR intensity, averaged over l and b , indicate that, on large angular scales, the observed SXR intensity variation is determined, in detail, by the distribution of the absorbing interstellar medium. The similarity between the observed and modelled SXR maps shows that small-scale intensity variations ($\leq 1^\circ$) of the observed SXR can also be attributed to photoelectric absorption. The soft X-ray absorption is well traced by HI in the velocity range

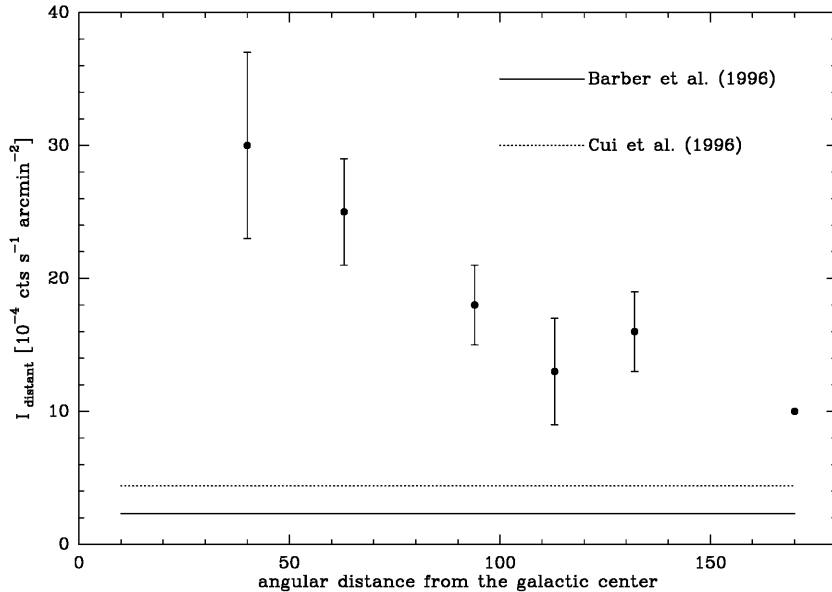


Fig. 7. Dependence of I_{distant} (dots) derived from our analysis on angular distance from the galactic center. The data point without an error bar corresponds to an averaged value extracted from the analysis of Herbstmeier et al. (1995). With the exception of this point, all I_{halo} intensities are towards comparable b . The horizontal solid and dashed lines represent the I_{extragal} intensity level based on Barber et al. (1996) and Cui et al. (1996), respectively. I_{distant} shows a continuous decrease with increasing angular distance from the galactic center and is significantly larger than I_{extragal} towards all analyzed fields.

$|v_{\text{LSR}}| \leq 100 \text{ km s}^{-1}$. This range covers the conventional galactic gas as well as the IVCs. Because the chosen velocity range includes low-velocity as well as intermediate-velocity HI, and because in some cases the HI column from the IVC gas exceeds that of the conventional-velocity gas, the X-rays have to originate beyond the IVCs studied by Kuntz & Danly (1996). From the soft X-ray shadow cast by HVC complex M (Herbstmeier et al. 1995), we conclude that at least a minor fraction of the galactic distant X-ray emission originates at distances larger than that of HVC complex M. We conclude that nearly all galactic HI absorbs the X-ray halo radiation, because the vertical extent of the galactic HI is entirely located within this distance range (Lockman & Gehman 1991).

Our analysis suggests that HI alone predominantly traces the X-ray absorption, because otherwise the modelled X-ray intensities would not fit the observational data as well as they do. H_2 certainly absorbs the SXR background radiation along some lines of sight, but is not diffusely distributed over scales of several tens of degrees, and is rare at the higher galactic latitudes considered here (Magnani et al. 1997). Furthermore, the SXR background source intensity absorption traced by H_2 occurs within regions of high N_{HI} , for instance as shown by our data towards the Polaris Flare (Sect. 4.1.2; Meyerdierks & Heithausen 1996). Otherwise we would have detected deep soft X-ray absorption features not traced by the N_{HI} distribution, because $\sigma_{\text{X}}(\text{H}_2) \geq 2 \cdot \sigma_{\text{X}}(\text{HI})$.

Soft X-ray absorption associated with diffusely distributed ionized hydrogen (Reynolds 1991) is also not obvious in our data. If the H^+ layer has a column density distribution similar to that of the HI layer, we would anticipate a constant scaling factor for the brightness of the galactic halo X-ray component. On the other hand, if the distribution of H^+ is patchy within the analyzed fields, its soft X-ray absorbing column density would be about $\Delta N_{\text{H}^+} \leq 7 \cdot 10^{19} \text{ cm}^{-2}$.

The low SXR background source intensity towards the galactic anticenter can be used to separate the contribution from galac-

tic halo emission and that from unresolved extragalactic point sources. Barber et al. (1996) determined $I_{\text{extragal}} = 2.3 \cdot 10^{-4} \text{ cts s}^{-1} \text{ arcmin}^{-2}$, while Cui et al. (1996) derived $I_{\text{extragal}} = 4.4 \cdot 10^{-4} \text{ cts s}^{-1} \text{ arcmin}^{-2}$. Our minimum $\frac{1}{4} \text{ keV}$ count rate is about $I_{\text{distant}} = (13 \pm 4) \cdot 10^{-4} \text{ cts s}^{-1} \text{ arcmin}^{-2}$. In the extreme cases $I_{\text{distant}}^{\text{min}} = 9 \cdot 10^{-4} \text{ cts s}^{-1} \text{ arcmin}^{-2}$ and $I_{\text{extragal}}^{\text{max}} = 4.4 \cdot 10^{-4} \text{ cts s}^{-1} \text{ arcmin}^{-2}$, the extragalactic X-ray background contribution is about equal to the soft X-ray intensity of the galactic halo. We plotted the I_{distant} values as a function of angular distance from the inner Galaxy in Fig. 7. The horizontal lines in the lower part of Fig. 7 indicate the extragalactic background level determined by Barber et al. (1996) and Cui et al. (1996). I_{distant} increases towards the galactic center. This leads us to conclude that the bulk of the distant soft X-ray emission is of galactic origin and that the extragalactic background radiation gives only a constant X-ray intensity offset.

5.2. X-ray enhancements near HVCs

We have shown that the general radiation transfer of the SXR photons is well represented by our modelling of the diffuse X-ray background. Our analysis of the ROSAT all-sky data reveals *no* evidence for soft X-ray shadows attributable to HVCs. This is in some respect surprising because our analysis is biased *towards the detection* of HVC soft X-ray *shadows* and, consequently, *against* the detection of soft X-ray *enhancements* of HVCs (see Sect. 3.5.2). Certainly, HVCs attenuate the extragalactic background radiation. As shown above, the maximum extragalactic background intensity is $I_{\text{extragal}} = 4.4 \cdot 10^{-4} \text{ cts s}^{-1} \text{ arcmin}^{-2}$ (Cui et al. 1996) and an HVC with $N_{\text{HI}}(\text{HVC}) = 1 \cdot 10^{20} \text{ cm}^{-2}$ attenuates this radiation by about 60%. If some HVCs are located at large distances from the galactic disk (see Blitz et al. 1998) this only HVC absorbed X-ray radiation is additionally attenuated by the diffuse galactic HI layer. This layer may be characterized by a

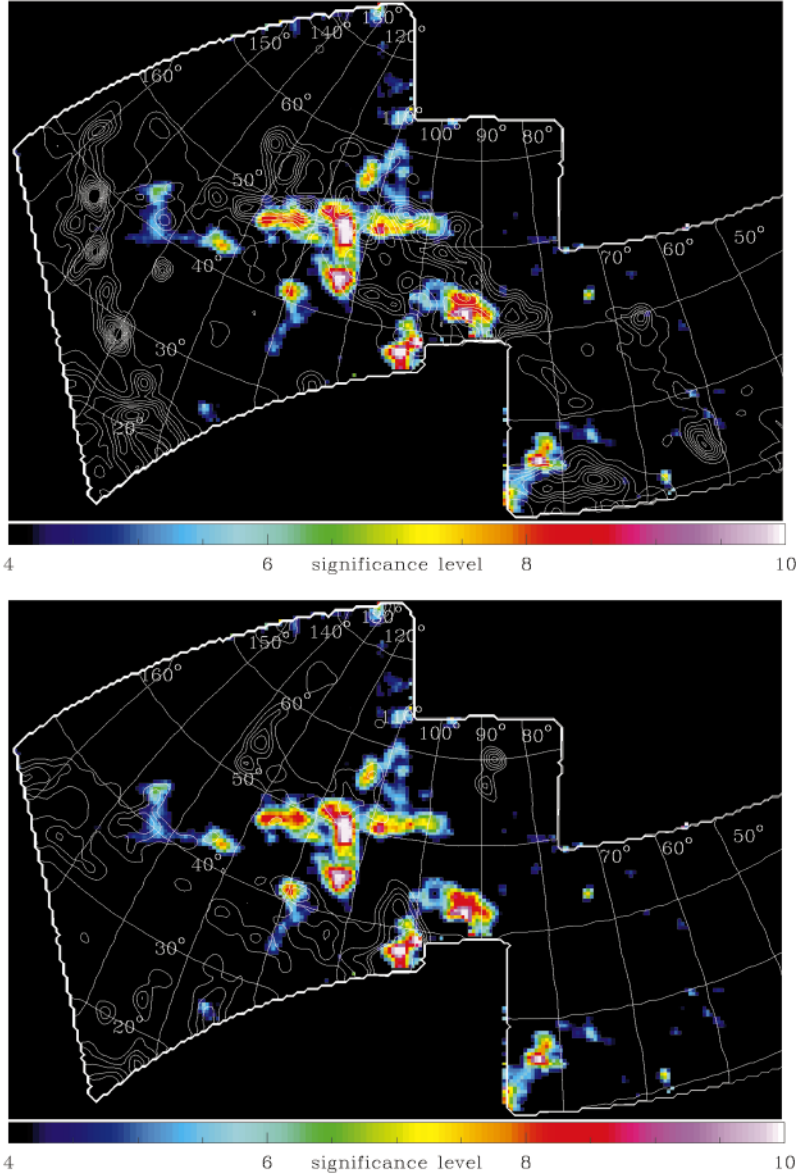


Fig. 8. Mosaic showing the positional correlation of excess $\frac{1}{4}$ keV emission and the HVC and IVC N_{HI} distributions towards the entire HVC complex C. The images present the areas of excess soft X-ray emission in the significance range 4σ (dark colour) to 10σ (bright colour). *Top:* The HVC N_{HI} distribution ($-450 < v_{\text{LSR}} < -100 \text{ km s}^{-1}$) superposed as contours with $1 \cdot 10^{19} \text{ cm}^{-2} \leq N_{\text{HI}} \leq 1 \cdot 10^{20} \text{ cm}^{-2}$ in steps of $\Delta N_{\text{HI}} = 1 \cdot 10^{19} \text{ cm}^{-2}$. *Bottom:* The IVC N_{HI} distribution ($-75 < v_{\text{LSR}} < -25 \text{ km s}^{-1}$) superposed as contours with $5 \cdot 10^{19} \text{ cm}^{-2} \leq N_{\text{HI}} \leq 2 \cdot 10^{20} \text{ cm}^{-2}$ in steps of $\Delta N_{\text{HI}} = 2.5 \cdot 10^{19} \text{ cm}^{-2}$. The HVC N_{HI} distribution follows the orientation of the soft X-ray enhancements. The IVCs reach N_{HI} maxima not positionally coincident with excess X-ray emitting areas, except near $l \sim 102^\circ$, $b \sim 37^\circ$, close to the Draco nebula, and near $l \sim 118^\circ$, $b \sim 42^\circ$. Both IVCs are located close to HVCs. In particular, the cloud at $l \sim 102^\circ$, $b \sim 37^\circ$ is close to an HI velocity bridge (VB 111+35, Pietz et al. 1996) which was not detectable in the higher l and b portion of HVC complex C (Sect. 4.1.2). A further investigation of the connection of IVCs and HVCs is mandatory.

typical N_{HI} of about $N_{\text{HI}}(\text{HVC}) = 1 \cdot 10^{20} \text{ cm}^{-2}$. On the HVC we observe a count rate of about $I_{\text{extragal}}(\text{ON}) = 0.9 \cdot 10^{-4} \text{ cts s}^{-1} \text{ arcmin}^{-2}$ whereas *off* the HVC the count rate is $I_{\text{extragal}}(\text{OFF}) = 1.7 \cdot 10^{-4} \text{ cts s}^{-1} \text{ arcmin}^{-2}$. The difference $I_{\text{extragal}}(\text{OFF} - \text{ON}) = 0.8 \cdot 10^{-4} \text{ cts s}^{-1} \text{ arcmin}^{-2}$ is undetectable in the *ROSAT* data analyzed at the current angular resolution.

For the HVC complexes C, GCN, and D we found significant soft X-ray emission close to or towards the HVCs. In case of the higher- l end of HVC complex C, soft X-ray enhancements up to the $11\text{-}\sigma$ level were detected. The X-ray enhancements generally follow the orientation of the HVCs, for instance in the case of HVC complex C (Fig. 4d), but not always in detail. In case of HVC complex C, large parts of the complex are located close to intermediate-velocity gas (Kuntz & Danly 1996). Depending on the origin of the excess soft X-ray radiation, IVCs may also be X-ray bright. To investigate this, we mosaicked the X-ray and HI

data of the entire HVC complex C. Fig. 8 shows a mosaic, where the excess soft X-ray emission is displayed in colour and the N_{HI} distribution of the HVCs ($-450 < v_{\text{LSR}} < -100 \text{ km s}^{-1}$) and IVCs ($-75 < v_{\text{LSR}} < -25 \text{ km s}^{-1}$) are superposed as contours. Contours of the HVC N_{HI} distribution encompass areas of excess X-ray emission (Fig. 8, *top*).

IVCs show a lower degree of correlation with the soft X-ray enhancements (Fig. 8, *bottom*) than shown by the HVCs (Fig. 8, *top*). Their HI emission maxima coincide positionally with minima in the X-ray emission, indicating that IVCs absorb the constant I_{distant} intensity distribution. Most probably, they are located nearer than the sources of the excess soft X-rays. Thus, HVCs remain as the most probable candidate for the association with the excess soft X-ray emission, while the role of the IVCs remains unclear. Especially the presence of the “velocity bridges” (Pietz et al. 1996) linking some HVCs with the excess X-ray emission with the intermediate-velocity gas

Table 3. Properties of the soft X-ray enhancements towards HVC complexes C, D and GCN. The l and b extent is determined by the distribution of the 4σ and 5σ contour lines, plotted in the individual maps of the fields of interest. E_{det} denotes the total energy detected by the *ROSAT* PSPC integrated across the extent of the excess soft X-ray emitting area. $\bar{\sigma}$ gives the mean significance level, while σ_{max} gives the maximum significance level within the extent of the excess emission area. To evaluate the emission measure (EM) as well as the electron volume density (n_e), we assumed $\log(T[\text{K}]) = 6.2$ (Kerp et al. 1998) and a “normalized” distance of $D = 1$ kpc to the HVCs. For a different distance of the HVCs the radiated 1/4 keV energy ($E_{\text{rad}}(1/4\text{keV})$) has to be scaled by D^2 [kpc] and the corresponding electron density by $D^{-0.5}$ [kpc]. The last two columns give the field-averaged significance level of the $\frac{1}{4}$ keV excess emission and the peak significance level.

complex	l -range	b -range	$E_{\text{det}}(1/4\text{keV})$ (10^{-11} erg cm $^{-2}$ s $^{-1}$)	$E_{\text{rad}}(1/4\text{keV})$ (10^{34} erg s $^{-1}$)	EM (cm $^{-6}$ pc)	n_e (cm $^{-3}$)	$\bar{\sigma}$	σ_{max}
C	143°–148°	42°–45°	5.4	5.0	0.054	0.03	5.0	6.3
C	129°–135°	41°–44°	6.2	4.2	0.041	0.03	5.8	7.8
C	119°–130°	46°–51°	21.7	6.7	0.022	0.01	6.3	8.5
C	116°–122°	39°–43°	7.3	3.9	0.034	0.02	5.6	8.2
C	110°–116°	41°–46°	11.6	4.5	0.032	0.02	7.1	10.2
C	110°–117°	46°–53°	23.4	8.1	0.033	0.02	7.7	11.2
C	110°–116°	54°–58°	7.5	2.4	0.022	0.02	5.5	7.8
C	97°–111°	50°–53°	28.5	7.6	0.031	0.02	6.5	9.0
C	99°–105°	35°–39°	5.2	6.7	0.044	0.02	6.6	11.0
C	89°–96°	41°–45°	14.7	3.9	0.024	0.02	6.7	10.6
D	80°–84°	23°–27°	3.7	2.4	0.028	0.02	6.6	10.1
GCN	34°–40°	–31°––28°	4.7	5.4	0.034	0.02	2.5	5.3

deserves further investigation, especially in regard to the Blitz et al. (1998) predictions.

The difference in location between the H I clouds and the soft X-ray emission is not surprising if we assume that the X-ray emitting plasma and the HVCs are spatially close. Under this hypothesis, the neutral HVC boundaries are ionized by the radiation from the X-ray plasma. This can cause the apparent positional shift between the neutral gas and the X-ray radiation. In consequence, H $^+$ radiation should be detectable from this interface region; in particular, it has to originate close to N_{HI} gradients. Towards complexes M, A, and C, Tuft et al. (1998) detected H α radiation. In these cases the soft X-ray enhancements reveal the presence of collisionally ionized gas.

These findings can be interpreted in two general ways. First, an H I gradient is caused by the ionizing radiation from the X-ray plasma alone (conductive interfaces). Second, an H I gradient is caused by the interaction of the HVC with the ambient ISM.

For HVC complex C (higher- l end, Sect. 4.1.2), we can estimate the energy budget of the apparent interaction process. Assuming that complex C has a total mass of about $M_{\text{HVC}} \sim 10^6$ to $10^7 M_{\odot}$ and a bulk velocity of $v_{\text{HVC}} \sim 100$ km s $^{-1}$ (Wakker & van Woerden 1991), the kinetic energy of the complex is $E_{\text{kin}}(\text{HVC}) \sim 10^{53}$ – 10^{54} erg. In the *ROSAT* $\frac{1}{4}$ keV band we detect at maximum $E_{\text{X}} \sim 10^{36}$ erg s $^{-1}$. Thus, the observed X-rays require only a very small fraction of the available kinetic energy. This implies that we need, from the energy point of view, only a weakly-efficient process which converts the HVC bulk motion into thermal energy. If the excess soft X-ray emission is caused by heating of the HVC and the surrounding medium, we have to investigate the physical conditions of the interaction scenario. At a vertical distance of $|z| \sim 3$ kpc, the temperatures are about $T \simeq 10^5$ – 10^6 K, the volume densities $n_{\text{HI}} \simeq 10^{-3}$ cm $^{-3}$ (Kalberla & Kerp 1998), and the sound

speed $v_s \simeq 40$ – 120 km s $^{-1}$. It is difficult to account for a strong shock if the absolute value of the complete HVC velocity vector is $|v_{\text{HVC}}| \sim 100$ km s $^{-1}$. Two other possibilities are open to overcome this distance discrepancy, namely the galactic wind scenario (Kahn 1991), in which a wind encounters the HVCs, and the magnetic reconnection process (Kahn & Brett 1993, Zimmer et al. 1997), in which turbulent motions within and close to the HVC disturb the magnetic lines of force. The field lines find a new configuration of minimum energy during the reconnection process. As Zimmer et al. (1997) pointed out, the magnetic reconnection can heat the ISM to several million degrees.

A remaining problem concerns the large angular extent of the areas of excess soft X-ray emission. As Fig. 4d shows, the angular extent of the soft X-ray excess emission and the extent of HVC complex C are about equal. Assuming a distance of at least 2 kpc for complex C, this corresponds to a linear size of at least 150 pc. Heating such a volume via atomic collisions would require $t_{\text{collision}} \sim 5 \cdot 10^6$ years. This time is comparable to the cooling time of the detected X-ray plasma. This may indicate that the thermal expansion of hot gas heated by a single event may not be the source of the observed X-ray radiation. We note that the Alfvén velocity is much higher than the sound speed: $v_A^2 = \frac{B^2}{4\pi n_{\text{HI}} m_{\text{p}}} \gg v_s$, where B denotes the magnetic field strength and n_{HI} the volume density of the medium. If $B = 3 \mu\text{G}$ (Beuermann et al. 1985) and $n_{\text{HI}} = 1 \cdot 10^{-3}$ cm $^{-3}$, then $v_A \simeq 200$ km s $^{-1}$. This indicates that the magnetic lines of force transfer information about the motion of the HVCs in the halo some five times more rapidly than the particle collisions do. Understanding the role played by magnetic fields may be important to understanding the HVC excess X-ray emission scenario.

6. Summary

We compared selected fields from the $\frac{1}{4}$ keV *ROSAT* all-sky survey against the Leiden/Dwingeloo H I survey looking for correlations between HVCs and soft X-ray emission. We considered the soft X-ray radiation transfer in detail towards several prominent HVC complexes. Our results show that:

1. The observed SXRb shows a smooth diffuse X-ray source intensity distribution at the higher latitudes (see Fig. 7).
2. Small- and large-scale ($0^{\circ}8 - 30^{\circ}$) variations of the observed SXRb distribution can be attributed to photoelectric absorption.
3. H I alone traces the amount of soft X-ray absorbing interstellar matter well.
4. Warm H I (i.e. the intercloud medium) traces most of the soft X-ray absorbing interstellar medium.
5. The intensity of the distant X-ray emission decreases with increasing angular distance to the galactic center, implying that most of the distant soft X-ray emission is galactic in origin. The distant SXRb shows comparable intensities on the northern and southern sky.
6. The distant soft X-ray emission probably consists of a superposition of a galactic X-ray plasma component ($T_{\text{plasma}} \sim 10^{6.3}$ K) and a component of unresolved extragalactic point sources. More than 50% of the total radiation observed towards the galactic anticenter can be attributed to the galactic halo plasma emission.

The above results are consistent with those of Pietz et al. (1998a; 1998b).

We detected the following deviations from the smooth distant galactic X-ray background intensity distribution towards several prominent HVC complexes:

1. Large portions of HVC complex C are positionally associated with excess soft X-ray emission.
2. Towards a part of HVC complex D, we detected enhanced soft X-ray emission, positionally associated with an HVC filament. However, we note that there is also an IVC close to this area of excess emission.
3. We detected enhanced soft X-ray emission in the direction of Mrk 509, where Sembach et al. (1995) found highly-ionized gas associated with HVC complex GCN.
4. Towards complex WA we found inconclusive evidence for excess X-rays.

Acknowledgements. J. Kerp thanks the Deutsche Forschungsgemeinschaft for support under grant No. ME 745/17-2. J. Pietz thanks the Deutsche Agentur für Raumfahrtangelegenheiten for support under grant No. 40012. The *ROSAT* project has been supported by the German Bundesministerium für Bildung, Wissenschaft, Forschung und Technologie (BMBF) and by the Max-Planck-Gesellschaft. We thank K.S. de Boer and the anonymous referee for comments based on careful readings of the manuscript.

References

- Almaini O., Shanks T., Boyle B.J. et al., 1996, MNRAS 282, 295
 Barber C.R., Roberts T.P., Warwick R.S., 1996, MNRAS 282, 157
 Beuermann K., Kanbach G., Berkhuijsen E.M., 1985, A&A 153, 17
 Blitz L., Spergel D.N., Teuben P.J., Hartmann D., Burton W.B., 1998, ApJ, submitted
 Cox D.P., Reynolds R.J., 1987, ARA&A 25, 303
 Cui W., Sanders W.T., McCammon D., Snowden S.L., Womble D.S., 1996, ApJ 468, 117
 Danly L., Albert C.E., Kuntz K.D., 1993, ApJ 416, L29
 Deul E.R., Burton W.B., 1990, A&A 230, 153
 Dickey J.M., Lockman F.J., 1990, A&AR 28, 215
 Egger R., Aschenbach B., 1995, A&A 294, L25
 Egger R., Freyberg M.J., Morfill G.E., 1996, Space Science Reviews 75, 511
 Freyberg M.J., 1997 in “The Physics of galactic Halos”, eds. Lesch H., Dettmar R.J., Mebold U., Schlickeiser R., Akademie Verlag Berlin, p. 117
 Gendreau K.C., Mushotzky R., Fabian A.C., et al., 1995, PASJ 47, 5
 Georgantopoulos I., Stewart G.C., Shanks T., Boyle B.J., Griffiths R.E., 1996, MNRAS 280, 276
 Hartmann D., Burton W.B., 1997, “Atlas of Galactic Neutral Hydrogen”, Cambridge University Press
 Hartmann D., Kalberla P.M.W., Burton W.B., Mebold U., 1996, A&AS 119, 115
 Hartmann D., Magnani L., Thaddeus P., 1998, ApJ 492, 205
 Hasinger G., 1991, in “X-ray emission from galactic nuclei and the cosmic X-ray background” eds. Brinkmann W., Trümper J.E., MPE-Report 235, p. 321
 Hasinger G., Burg R., Giacconi R., et al., 1993, A&A 275, 1
 Hasinger G., Burg R., Giacconi R., et al., 1998, A&A 329, 482
 Herbstmeier U., Mebold U., Snowden S.L., et al., 1995, A&A 298, 606
 Herbstmeier U., Kalberla P.M.W., Mebold U., et al., 1996, A&AS 117, 497
 Heithausen A., Thaddeus P., 1990, ApJ 353, 49
 Heithausen A., Stacy J.G., de Vries H.W., Mebold U., Thaddeus P., 1993, A&A 268, 265
 Hirth W., Mebold U., Müller P. 1985, A&A 153, 249
 Kahn F.D., 1991, IAU Symp. 144, “The disk-halo connection” ed. Bloemen H., p. 1
 Kahn F.D., Brett L., 1993, MNRAS 263, 37
 Kalberla P.M.W., Kerp J., 1998, A&A in press
 Kerp J., 1994, A&A 289, 597
 Kerp J., Herbstmeier U., Mebold U., 1993, A&A 268, L21
 Kerp J., Lesch H., Mack K.-H., 1994, A&A 286, L13
 Kerp J., Lesch H., Mack K.-H., Pietz J.: 1995, Adv. in Space Res. Vol. 16, No. 3, 119
 Kerp J., Mack K.-H., Egger R., Pietz J., Zimmer F., Mebold U., Burton W.B., Hartmann D., 1996, A&A 312, 67
 Kerp J., Pietz J., 1998, IAU Coll. 166 “The Local Bubble and Beyond”, eds: Breitschwerdt D., Freyberg M.J., Trümper J., Lecture Notes in Physics 506, 337
 Kerp J., Pietz J., Kalberla P.M.W. et al. 1998, IAU Coll. 166 “The Local Bubble and Beyond”, eds: Breitschwerdt D., Freyberg M.J., Trümper J., Lecture Notes in Physics 506, 457
 Kuntz K., Danly L., 1996, ApJ 457, 703
 Lockman F.J., Gehman C.S., 1991, ApJ 382, L182
 Lockman F.J., Jahoda K., McCammon D., 1986, ApJ 302, 432
 Marshall F.J., Clark G.W., 1984, ApJ 287, 633
 Magnani L., Hartmann Dap, Speck B.G., 1996, ApJS 106, 447
 McCammon D., Sanders W.T., 1990, ARA&A 28, 657

- Meyerdierks H., Heithausen A., 1996, A&A 313, 929
- Meyerdierks H., Heithausen A., Reif K., 1991, A&A 245, 247
- Morrison R., McCammon D., 1983, ApJ 270, 119
- Pfeffermann E., Briel U.G., Hippmann H. et al., 1986, Proc. of SPIE 733, 519
- Pietz J., Kerp J., Kalberla P.M.W., et al., 1996, A&A 308, L37
- Pietz J., Kerp J., Kalberla P.M.W., et al., 1998a, IAU Coll. 166 “The Local Bubble and Beyond”, eds: Breitschwerdt D., Freyberg M.J., Trümper J., Lecture Notes in Physics 506, 471
- Pietz J., Kerp J., Kalberla P.M.W., Mebold U., Burton W.B., Hartmann D., 1998b, A&A 332, 55
- Plucinsky P.P., Snowden S.L., Briel U.G., Hasinger G., Pfeffermann E., 1993, ApJ 418, 519
- Raymond J.C., Smith B.W., 1977, ApJS 35, 419
- Reynolds R.J., 1991, IAU Symp. 144, “The disk-halo connection” ed. Bloemen H., p. 67
- Rocchia R., Arnaud M., Blondel C., et al., 1984, A&A 130, 53
- Sembach K.S., Savage B.D., Lu L., Murphy E.M., 1995, ApJ 451, 616
- Sidher S.D., Sumner T.J., Quenby J.J., Gambhir M., 1996, A&A 305, 308
- Snowden S.L., Freyberg M.J., 1993, ApJ 404, 403
- Snowden S.L., Schmitt J.H.M.M., 1990, Ap&SS 171, 207
- Snowden S.L., Egger R., Freyberg M.J., et al., 1997, ApJ 485, 125
- Snowden S.L., Egger R., Finkbeiner D.P., Freyberg M.J., Plucinsky P.P., 1998, ApJ 493, 715
- Snowden S.L., Freyberg M.J., Plucinsky P.P., Schmitt J.H.M.M., Trümper J., Voges W., Edgar R.J., McCammon D., Sanders W.T., 1995, ApJ 454, 643
- Snowden S.L., Hasinger G., Jahoda K., et al., 1994b, ApJ 430, 601
- Snowden S.L., McCammon D., Burrows D.N., Mendenhall J.A., 1994a, ApJ 424, 714
- Tufte S.L., Reynolds R.J., Haffner L.M., 1998, ApJ, in press
- van Woerden H., Wakker B.P., Schwarz U.J., Peletier R., & Kalberla P.M.W., 1998, IAU Coll. 166 “The Local Bubble and Beyond”, eds: Breitschwerdt D., Freyberg M.J., Trümper J., Lecture Notes in Physics 506, 467
- Voges W., 1992, in proc. of Satellite Symp. 3, eds. Guyenne T.D., Hunt J.J., (Noordwijk: ESA Publication Division), 9
- Wakker B.P., van Woerden H., 1991, A&A 250, 509
- Wakker B.P., van Woerden H., 1997, ARA&A 35, 217
- Wang Q.D., 1998, IAU Coll. 166 “The Local Bubble and Beyond”, eds: Breitschwerdt D., Freyberg M.J., Trümper J., Lecture Notes in Physics 506, 503
- Wannier P., Wrixon G.T., Wilson R.W., 1972, A&A 18, 224
- Welsh B.Y., Crifo F., Lallement R., 1998 A&A 333, 101
- Wennmacher A., Lilienthal D., Herbstmeier U., 1992, A&A 261, 9
- Zimmer F., Lesch H., Birk G.T., 1997, A&A 320, 746